Abstract of "Electrokinetic noise driven dynamics of DNA molecules and dynamics of nanoparticles in diffusivity gradients. "
Shayan Lameh, Brown University, May 2023.

This dissertation presents a new technique to increase the accessible noise range in micro and nanofluidics using electrokinetics. We show that the application of voltage noise with the same statistical properties as fundamental thermal noise controllably amplifies the Brownian motion of lambda DNA molecules suspended in solution inside a nanoslit. We analyzed the trajectories of single molecules and found that their self-diffusivity in the direction of the applied electric field increased in proportion with the variance of the voltage noise. However, unlike thermal noise, the voltage noise causes correlated fluctuations of different molecules and their segments. Therefore, this technique unlocks a previously inaccessible effective temperature regime for studies and applications of noise-dependent phenomena. Using this new technique, we significantly increased the back and forth hopping of a DNA between neighboring nanopits inside a nanofluidic device.

The second half of this dissertation presents observation, analysis, theory, and simulation of a new nanofluidic transport phenomenon where a gradient in liquid viscosity causes transport of nanoparticles inside a glass nanofluidic channel. Viscosity gradient results in multiplicative (state-dependent) noise, which refers to the dependence of a particle's thermal fluctuations on its position. To investigate the motion of particles in viscosity gradient we measured the drift and the flux of nanoparticles as well as the ionic current inside the nanochannel with no applied voltage, pressure, or salinity gradient. We show that the resulting dynamics agrees with the isothermal description for Brownian particles. We discuss the origins of the ionic current, the dynamics of the nanoparticles, and the role of the boundary conditions for the ions and the nanoparticles.

"Electrokinetic noise driven dynamics of DNA molecules and dynamics of nanoparticles in diffusivity gradients. "

By
Shayan Lameh
B.Sc., University of California Santa Barbara, 2014
M.Sc., Brown University, 2017

Dissertation
Submitted in partial fulfillment of the requirement for the Degree of Doctor of Philosophy in the Department of Physics at Brown University

PROVIDENCE, RHODE ISLAND
May 2023

This dissertation by Shayan Lameh is accepted in its present form by the Department of Physics as satisfying the dissertation requirement for the degree of Doctor of Philosophy.

Derek, Stein, Director Date

Professor of Physics

Kosterlitz, Michael, Reader Date

Professor of Physics

Valles, James, Reader Date

Professor of Physics

Thomas A. Lewis, Dean of the Graduate School Date

ACKNOWLEDGMENTS

This thesis represents an original published and unpublished collaborative effort between myself and my adviser, Prof. Derek Stein

Many thanks to my adviser, Derek Stein, who believed in me and taught me about the interesting field of single molecule biophysics and nanofluidics. I would also like to thank Professor Jay Tang my academic advisor, Daniel Kim, who offered guidance and trained me in my research, and my group mates Nicholas Drachman, Liam Storan, Jerry Ding, and Tim Zhao for their help. Finally, thanks to the Brown University Physics Department for awarding me a Dissertation Fellowship to write this dissertation.

Contents

1 Introduction **9**

1.1 Noise and its manifestations 9

1.2 Beneficial roles of noise in physical systems 11

1.3 Brownian motion: a manifestation of thermal fluctuations 12

1.4 Kramers' theory of barrier hopping 14

1.5 Multiplicative noise and the Itô-Stratonovich dilemma 14

1.6 Nanofluidics as an arena in which to study noise driven phenomena 19

1.7 Outline of the dissertation 19

2 Experimental and analytical methods **23**

2.1 Overview and fabrication of nanofluidic devices 23

2.1.1 Substrate preparation 24

2.1.2 Patterning and etching a nanoslit and microchannels 25

2.1.3 Patterning and etching nano-pits 26

2.1.4 Creating sealed devices with access holes 26

2.2 System for applying an arbitrary time-dependent pressure difference 27

2.3 System for applying an arbitrary time-dependent voltage difference 28

2.4 Preparation of the nanofluidic device for an experiment 29

2.5 Tracking individual particles and DNA molecules 30

2.5.1 Fluorescence microscopy 30

2.5.2 Image analysis techniques 31

3 Controlled Amplification of DNA Brownian Motion Using Electrokinetic Noise 33

3.1 Overview: DNA Brownian motion due to thermal and electrokinetic noise . . 33

3.2 Methods 38

3.2.1 Preparation of fluorescently stained DNA 38

3.2.2 Dimensions of the nanofluidic device 38

3.2.3 DNA tracking procedure 38

3.3 Results and interpretations: DNA diffusivity as a function of the applied electrokinetic noise 40

3.4 Concluding remarks 45

4 Noise Assisted Barrier Crossing of DNA Molecules in a Nanofluidic Environment 47

4.1 Overview: from Kramer's reaction rate theory to DNA barrier hopping. . . . 47

4.2 Experimental setup: characteristics of the bistable entropic trap and the applied electrokinetic noise 48

4.3 Simulations of a Brownian particle in a bistable potential 50

4.4 Results: DNA hopping rate as a function of the applied electrokinetic noise . 54

4.5 Discussions: shortcomings of the Arrhenius model in describing the DNA hopping rate over an entropic trap. 57

4.6 Concluding remarks 60

5 Viscosity Driven Drift of Nano-sized Particles in a Nanofluidic Environment 63

5.1 Theoretical foundation and previous work on transport in diffusivity gradients 63

5.2 Experiment overview and methods 66

5.3 Results: fluorescent particles dynamics and ionic current. 70

5.4 Discussion and interpretation 76

6 Conclusions: Summary of what we learned, possible future work and open questions 79

Chapter 1

Introduction

1.1 Noise and its manifestations

The word "noise" is widely used in acoustics and is referred to random series of tones of wide range of frequencies. However, the word noise is not limited to acoustics; it is widely used in physical sciences and technology as well. There is a close analogy between acoustical noise and random fluctuation phenomena like those encountered in Brownian motion. It is on this analogy that the use of the word "noise" in current physical literature and this dissertation is based [1].

Noise in this context manifests itself in many forms and plays a central role in a broad range of fields and phenomena. In climate systems, noise refers to the short term temperature fluctuations that have little or no organized structure in time or space whereas the predictable seasonal patterns [2]. Although in principle weather patterns obey deterministic equations like the Naiver-Stokes equation, the high level of noise and sensitivity to the initial conditions makes the prediction of the weather very difficult over weeks or even a few days [3–5]. The high level of sensitivity to the initial conditions is also known as the butterfly effect: nearly 45 years ago, Edward Lorenz, a meteorology professor posed a question: "Does the flap of a butterfly's wings in Brazil set off a tornado in Texas?" The purpose of this question was

to illustrate that in some complex dynamical systems a small amount of uncertainty in the initial conditions could result in widely different and unpredictable outcomes. In financial markets, noise is in the form of price fluctuations, also called volatility which distorts the overall trend price (signal) [6]. One of the early discussions on the concept of noise in finance was in a paper titled "noise" in 1986 by economist Fischer Black, where he stated that "noise" should be distinguished from "information" and that a disproportionate amount of trading occurs based on noise, rather than information and evidence [6]. In this sense, understanding market noise is crucial for investors in order to distinguish what is driving the trend; whether a trend is changing or merely experiencing short-term volatility.

In fluids, noise is ubiquitous in the form of thermal fluctuations which cause apparently random motions for small particles submerged in them called Brownian motion [7] and plays a central role in many fluidic phenomena. For example, thermal fluctuations are crucial for chemical reactions to take place: some or all of the chemical bonds in the reactants must break in order for new bonds to form. Rearranging bonds requires molecules to overcome an energy barrier, called the activation energy. The source of activation energy comes from thermal fluctuations of the environment. Increasing the thermal fluctuations speeds up the motion of the reactant molecules, increasing the frequency and strength of their collisions which facilitates and speeds up the chemical reaction [8–10]. The core of this dissertation focuses on noise in fluids.

Across many fields, various techniques have been used to remove noise from signals in order to extract useful information about that system [11]. However, noise is not always unwanted or an experimental nuisance. Next section describes example phenomena where noise is beneficial [12, 13].

1.2 Beneficial roles of noise in physical systems

One interesting example where noise plays a beneficial role is stochastic resonance (SR). SR is a counter-intuitive phenomenon where the addition of white noise to a bi-stable system enhances the system's response to a weak external periodic driving force. A system that displays such behavior is called a stochastic resonator. This optimization can be useful to detect otherwise undetectable weak signals [13–16].

The hallmark of stochastic resonance is a peak in the response of that system with respect to the noise intensity. In another word, the existence of an optimum noise intensity Fig.1.1. It is worth noticing that since SR is observed in many different dynamical systems, from electromagnetism to biological systems [17–21], the response function varies widely, it could be the signal-to-noise-ratio or the synchronization of the registered output with the weak periodic input, or some other forms.

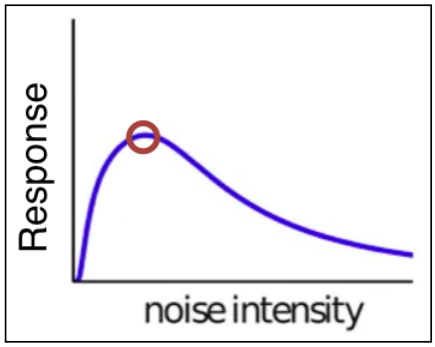

Figure 1.1: A typical plot of stochastic resonance. The response function peaks at an optimum noise intensity [22].

Furthermore, noise in the form of thermal fluctuations plays an important role in various phenomena taking place in micro and nanofluidic environments. It gives rise to the Brownian motion of suspended particles [7,23], osmotic pressure [24], the elasticity of polymers [25–27], and transport in heterogeneous media [28,29]. Having access to a large range of noise levels in fluidics allows us to study various interesting noise driven phenomena, however if we exclusively rely on thermal fluctuations as the source of noise, the freezing and boiling points

of water severely restrict the range in which the noise level can be experimentally varied. While traditionally, noise level in fluidics is set by the temperature (the strength of thermal fluctuations), a focus of this dissertation is to introduce a technique that mimics thermal fluctuations and controllably increases the accessible noise range in fluidic environments independently of temperature.

1.3 Brownian motion: a manifestation of thermal fluctuations

Chapter three and four report the increase in the diffusivity of DNA due to the increase in the noise range and chapter five investigates the dynamics of nanoparticles in a viscosity gradient. The motion of such small particles in fluids is commonly modeled by Brownian motion whose scale is set by the noise magnitude. Brownian motion of suspended particles links the macroscopic world to the microscopic world of molecules. Brownian motion is named after Robert Brown who in 1827 noticed the continuous motion of pollen suspended in water [30]. Initially he assumed a living organism must be behind the motion [31, 32]. However, by mid 19th century, scientist realized that Brownian motion is connected to temperature and accepted that living organisms are not behind Brownian motion. In 1905, Einstein proposed a theory explaining Brownian motion: small random bumps from interactions with the surrounding molecules are responsible for the continuous random motion of particles submerged in them. Einstein introduced the relation $D = \frac{k_B T}{6\pi\eta r}$, where D is the diffusion coefficient, $k_B T$ is the thermal energy and r is the hydrodynamic radius of the diffusing particle [33]. Within a few years, experiments proved Einsteins theory correct [34, 35].

Brownian motion plays a central role in a variety of phenomena in physics [36] , chemistry [9], biology [37], and technology [38, 39], and mathematical models of Brownian motion are

usefully applied to social and financial phenomena [40–43].

Mathematically speaking, Brownian motion can be modeled as a random walk whose step size is set by the strength of the thermal noise. One dimensional simple random walk is a good starting point. A simple random walker takes steps at a constant length with equal probability of stepping to the left or right. This means the position, x, changes by a fixed amount, L, in either the positive or negative direction, $\Delta x_i = r_i L$ where r is either 1 or -1. This leads to:

$$x_n = \Sigma_{i=0}^{n} \Delta x_i = \Sigma_{i=0}^{n} r_i L, \tag{1.1}$$

Where n is total number of steps. The average random walk is then,

$$< x_n >= L\Sigma_{i=0}^{n} < r_i >= 0, \tag{1.2}$$

The brackets represent the average over different realizations of that random variable. However, the average of the square of the displacement is not zero,

$$< x_n^2 >= L^2 \Sigma_{i,j=0}^{n} < r_i, r_j >, \tag{1.3}$$

r_i are uncorrelated, $< r_i, r_j >= \delta_{ij}$, so we can rewrite:

$$< x_n^2 >= L^2 = nL^2. \tag{1.4}$$

Since $n = t/\Delta t$ we can rewrite:

$$< x_n^2 >= \frac{tL^2}{dt} = 2Dt \tag{1.5}$$

where $D = \frac{L^2}{2dt}$ is the diffusion coefficient that characterizes the magnitude of the particle's fluctuations.

1.4 Kramers' theory of barrier hopping

Kramers used the concept of Brownian motion to describe the motion of particles over a barrier. According to Kramers theory, the rate, K, of barrier crossing for a particle moving in an external potential is described by the Arrhenius model of chemical reactions. In Arrhenius model, reactions are described by diffusion of a Brownian particle over a free-energy barrier separating reactants and products.

$$K = K_0 \exp\left[-\frac{\Delta G^{\dagger}}{k_B T} \right], \tag{1.6}$$

where K_0 is the attempt rate and $\Delta G^{\dagger}$ is the barrier height, and T is noise in the system which can equally represent non-thermal noise sources. This illuminates ways on increasing the noise range independently of temperature.

Chapter 4 describes a study where electrokinetic voltage noise is used to increase the noise assisted barrier hopping for DNA molecules back and forth inside an entropic double potential. The rates are obtained from the flux over barrier along reaction coordinate. While Kramers' theory is the leading approach to describe diffusive barrier crossing, the model only considers a fixed free energy barrier between two stable states, without accounting for the distance between them or the time it takes an object to travel that distance. We discuss the shortcomings of Arrhenius model to describe the barrier crossing dynamics for the DNA molecules in our experiments and suggest a numerical model that overcomes this limitation.

1.5 Multiplicative noise and the Itô-Stratonovich dilemma

Previous chapters mathematically showed that for particles in typical homogeneous media, Brownian motion results in no net motion. However, an ambiguity arises for Brownian particles in non-homogeneous media in which D varies with position. In this case, the

differential of the position x, can be written as

$$dx = x_{t+dt} - x_t = \sqrt{2D(x)}dW_t. \tag{1.7}$$

Intuitively, one might think that a diffusivity gradient should cause no net motion for submerged particles since diffusivity does not change the potential energy of a particle. It is also reasonable to think that a particle will drift towards lower diffusivity where it gets stuck more and more into the sticky side. Finally, one might think that a particle will escape into regions of high diffusivity, where mobility is higher and steps are larger.

Mathematically speaking, there is an ambiguity in calculating dx. To calculate dx, one needs to evaluate $D(x)$, but at what x? $D(x)$ varies along each step so do we evaluate $D(x)$ at the beginning of the increment, $D(x_t)$, at the end of the increment, $D(x_{t+dt})$, or somewhere in between? It turns out any choice of $D(x)$ along the step is mathematically valid but with significantly different physical consequences. [44–48]. This is known as the Itô-Stratonovich dilemma. While any choice of D(x) along a step is valid, Itô, Stratonovich, and isothermal are two special cases; the Itô integration rule determines each increment dx based on the value of $D(x)$ at the start of the increment, i.e. $D(x_t)$ [49]. This results in no preference for the particles to drift in either direction. The Stratanovich rule evaluates each increment at the midpoint [50, 51]); $D\ (x_t + \frac{\Delta t}{2})$. Finally, the isothermal rule bases the step size on the endpoint; $D(x_{t+\Delta t})$ [52]. In this case, particles take larger average steps in the direction of increasing D, resulting in a mean drift toward higher diffusivity. This is illustrated in Fig. 1.2.

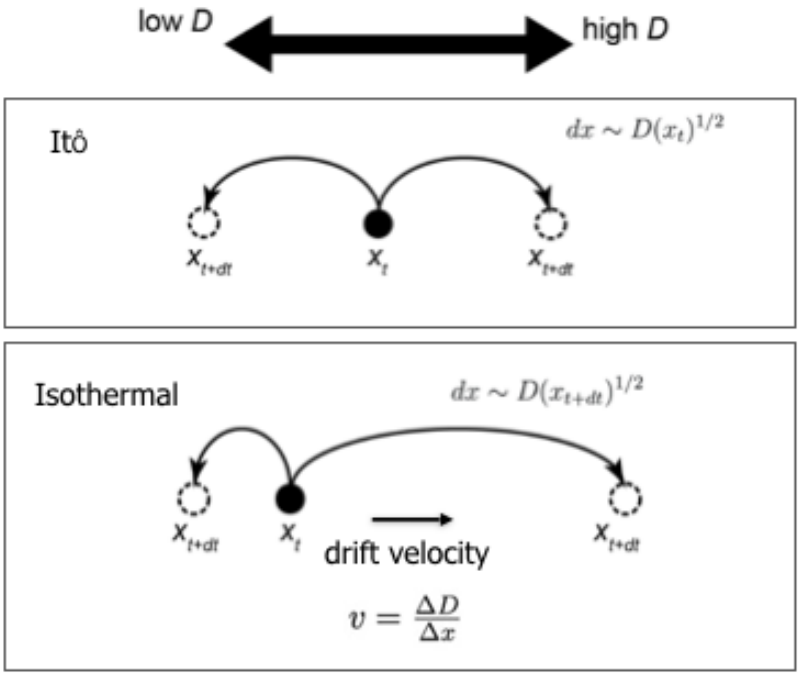

Figure 1.2: Illustrating drift according to the Itô and the isothermal conventions for a particle at position x at time t in a diffusivity gradient. The Itô convention results in no drift while the isothermal convention results in a drift of particles towards higher diffusivity

We can derive the drift velocity of a Brownian walker in a diffusivity gradient by rewriting Eq. 1.7 as $dx = \sqrt{2D(x + \alpha dx)}dW_t$, where α runs from 0 to 1. This allows us to set the integration convention through the choice of α. The special cases of Itô, Stratonovich, and isothermal rules correspond to $\alpha = 0$, $1/2$, and 1, respectively. The first step is to expand D(x + α dx) and rewrite dx as:

$$dx = \sqrt{2D(x)}dW_t + \alpha\frac{dD(x)}{dx}dW_t^2.$$

Taking the expectation value:

$$dx = x_{t+dt} - x_t =< \sqrt{2D(x)} >< dw_t > +\alpha < dD(x)/dx >< dw_t^2 >=$$
$$< x_{t+dt} >=< x_t > +\alpha < dD(x)/dx > dt$$
$$\langle \dot{x} \rangle = \alpha < dD(x)/dx > .$$

Setting $\alpha = 1$ gives the expected drift under the isothermal integration rule while $\alpha = 0$ predicts no drift for the Itô integration convention.

Furthermore, depending on the integration convention, the particles experience net flux or no flux. It comes down to how the Fick's Law of diffusion, $J = -D\Delta P(x)$, is generalized when D varies with position. Fick's Law related flux to the gradient of the concentration gradient where particles go from higher to lower concentration. J is the diffusion flux where the dimension is substance per unit area per unit time. P is the concentration of the diffusing particles, were the dimension is amount of substance per unit volume and x is the position, the dimension of which is length. One option, sometimes called the Fokker-Planck generalization, is to put the gradient operator outside the diffusivity and write $J = -\Delta(D(x)P(x))$. This results in an explicit flux term proportional to the diffusivity gradient, $-P(x)\Delta D(x)$. In this case when $J = 0$, $\Delta P(x) = \frac{P(x)}{D(x)}\Delta D(x)$. Another generalization is to leave the gradient operator inside the diffusivity and write $J = -D(x)\Delta P(x)$. This results is no explicit flux dependence on the diffusivity gradient. Therefore, when $J = 0$, $\Delta P(x)$ has to be zero. Figure 1.3 illustrates the predicted flux for the Itô and the isothermal conventions by showing the net crossings of an arbitrary plane inside a diffusivity gradient.

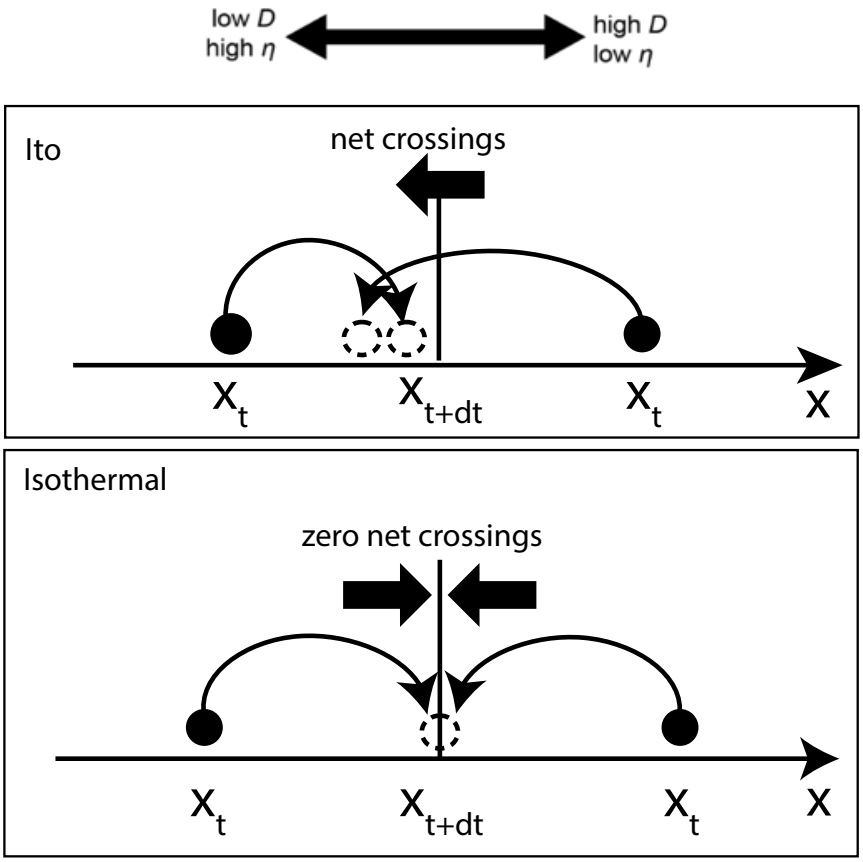

Figure 1.3: Illustrating flux for the Isothermal and Itô conventions, for a particle at position x at time t in a diffusivity gradient.

It is important to know which law governs a given physical system. Do particles in a liquid viscosity gradient drift? Is there a net flux? If so, which direction is the net flux and in what direction do they drift? Theoretically, the isothermal formulation is favored since it is the only formulation that respect the Boltzmann distribution of thermodynamics at equilibrium [47]. For example, for particles inside a diffusivity gradient inside a fluidic channel, this means that when there is no chemical potential gradient, Brownian particles should not experience a flux and accumulate at one end of the channel. Another focus of this dissertation is to experimentally explore this ambiguity for nano particles in a diffusivity gradient inside a nanochannel by directly measuring their drift and flux. Figure 1.3 illustrates the flux according to the it$\hat{o}$ and isothermal conventions.

1.6 Nanofluidics as an arena in which to study noise driven phenomena

All experimental work described in this dissertation takes place using nanofluidics. Nanofluidics is the science and technology of manipulating and controlling fluids, usually in the range of nano- to pico-liters in networks of nano-sized channels. Nanofluidic devices are nanoscale structures that can confine nanoscopic volumes of fluids and particles in geometries that can be arbitrarily shaped by nanofabrication. The micro and nanoscopic size of the structures reduce the sample consumption and shortens the equilibration times [53]. Additionally nanofluidic devices provide the necessary features with the correct scale to study individual nano- and micro-scale particles and molecules such as the DNA molecule.

The nanofluidics field started by groups of Austin aiming to create an ideal porous medium, as a substitute for the gel in electrophoresis and then Craighead, seeking to separate DNA molecules by length [54–56]. Nanofluidic devices have been widely used in biology and have opened up the possibility to probe biology on a single molecular scale where fundamental biological processes take place with potential applications in DNA sequencing [57], gene therapy [58, 59], and drug delivery [60]. Furthermore, by customizing the topography of a nanofluidic device, one can tailor the entropic landscape experienced by small particles and molecules such as the DNA and study entropic phenomena at single molecular level [61–65].

1.7 Outline of the dissertation

This dissertation consist of 6 chapters. Chapter 2 goes over the experimental and analytical methods used in the the following chapters. Some of the experimental and analytical methods that are more specific to a single project are left out of this chapter and will be discussed along with the project itself.

Chapter 3 describes a technique to controllably increase the effective noise experienced

by DNA molecules in micro and nanofluidic environments. We show that the application of voltage noise with the same statistical properties as fundamental thermal noise can amplify the Brownian motion of lambda DNA molecules suspended in solution inside a nanoslit. We analyze the trajectories of single DNA molecules and report that their self-diffusivity in the direction of the applied electric field increases in proportion with the variance of the voltage noise.

Chapter 4 presents and experimental and theoretical study of the dynamics of DNA molecules driven by artificial electrokinetic noise back and forth between neighboring nanopits inside a nanofluidic device. We show that the dynamics are consistent with a noise-assisted barrier crossing process, exhibiting a rapid increase in the hopping rate with noise level beyond a threshold. We argue that while a simple Arrhenius model with a fixed energy barrier of several k_BT describes the hopping dynamics well at low noise levels, but to accurately describe the dynamics over a wider range, we need a numerical model that additionally accounts for the lateral extent of the free energy landscape. Finally, we provide a numerical model of the DNA dynamics that additionally accounts for the lateral extent of the free energy landscape.

In chapter 5 we study the dynamics of nanoparticles in a diffusivity gradient, where noise is state-dependent. We created a diffusivity gradient across a nanochannel by imposing a viscosity difference across it. A viscosity gradient was created by intermixing fluids of different viscosities inside the nanofluidic channel. We measured the diffusivity profile and show that the viscosity gradient creates a linear diffusivity gradient along the channel. The goal of this chapter is to measure the drift and the flux of the particles inside the diffusivity gradient and compare it to different conventions and show that the particles experience a drift inside the nanochannel but no flux, which is consistent with the isothermal description of Brownian motion. Additionally, we measured an ionic current proportional to the viscosity imposed

and discuss that the boundary conditions for the particles plays an important role in their dynamics.

The sixth and final chapter is the conclusion of this dissertation. This chapter is a summary of what is learned and what is left to explore and potential applications.

Chapter 2

Experimental and analytical methods

2.1 Overview and fabrication of nanofluidic devices

This dissertation reports different dynamical phenomena that can be explored with sets of nanofluidic devices. In chapter 3 you will be looking at a nanofluidic devices with a 100 nm deep nanoslit in which the diffusion of DNA molecules is recorded. In chapter 4, two neighboring nano-sized pits create a bistable entropic trap for DNA molecules inside a nanoslit and allow us to study barrier hopping between them. In chapter 5, a mixing nanoslit attached to two microchannels allows fluids of different viscosities to mix and created a viscosity gradient for further studies. The basic geometry of all the devices is as follows: 4 reservoirs, 2 on each side of a nanoslit. Reservoirs are connected through 2 U-shaped

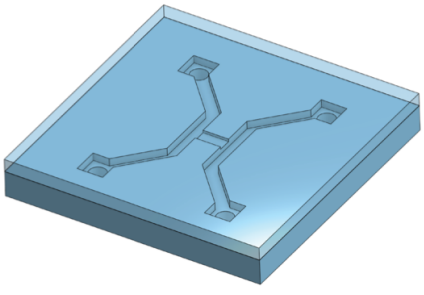

Figure 2.1: A 3D graphic of a finished chip illustrating the two microchannels, the nanoslit in between, and the access holes.

microchannels to the nanoslit as shown in Fig. 2.1. All the experiments happen inside the nanoslits. The technology for nanofabrication was initially developed to create high precision micro-electromechanical systems (MEMS). Nowadays, bio MEMS, Lab-on-a-Chips device and micro and nanofluidic devices are being explored using same advancements in nanotechnology [66].

I used common nanofabrication methods that were previously developed and used in our group. The freshness of the chemical used in each step of the fabrication was crucial for a successful outcome. Deposition, dry etch, and dimension measurements were done in a cleanroom of class 1000 while spin coating photolithography and bonding were done in a class 100 cleanroom.

2.1.1 Substrate preparation

Each device is made of two one-inch square silica chips (Marc Optics). The glass chips containing the etched patterns were thermally bonded with a thin cover slip to enclose the slit, channels, and reservoirs. Each round of fabrication started with five chips, one chip was always used to calibrate and test each step of the process as the timing and the rates of the instruments can vary over time. On average, three out of five chips resulted in a fully functional device.

First step was to clean any potential organic compounds. To do so, the chips were sonicated in 50% nitric acid for 10 minutes followed by a DI water rinse, then blow dried by an N_2 gun. To protect the surface of the chips, 50 nm of chromium using Kurt J. Lesker's thin film deposition systems with a rate of 0.9 to 1.1 Å/s was deposited on each chip. Then again for cleaning purposes, the chips were sonicated for 15 minutes in acetone (acetone dissolves most organic compounds), 15 minutes in isopropanol, followed by 15 minutes of DI water rinse, we call this a standard clean.

2.1.2 Patterning and etching a nanoslit and microchannels

Nanoslits, microchannels, and reservoirs were patterned using Karl Suss MJB-3 Mask Aligner ultraviolet (UV) lithography. The nanoslit was patterned and etched first, next the microchannels and the reservoirs were pattered and etched together. First, a layer of photoresist, S-1818 (Shipley) was spun on the entire chip with speed set to 4000 RPM for 30s (adopted from previous lab members), followed by a bake on the hot plate for 2 minutes at 110 C degree. Patterning was done using a patterning mask. The mask covered the chip but left a slit shape opening exposed to the UV radiation. As a result, the exposed part of the photoresist becomes soluble in the appropriate developer solution. Exposed wafer was developed in MF312:H_2O = 1:1 mixture for 60secs removing the photoresist on the slit and then dipped in water for 30secs to stop the process, and then dried by an N_2 gun. The patterned slit was checked using an optical microscope to ensure full removal of the resist. The underlying exposed chromium was then removed using Chromium etch and the slit was etched into the silica chip using a reactive ion etch (RIE) procedure, 4 minutes for slit of height 110-120 nm while the remaining chromium and photoresist protected the rest of the chip. The test chip was used to calibrate the time needed for removal. Next, all of S-1818 was removed through standard cleaning.

A new layer of resist was spun and the same process was repeated to pattern the microchannels this time with a different mask that exposed a channel pattern to UV light during photolithography. Microchannels were etched for 15 minutes resulting in 550 nm deep channels. Since the RIE rate can change over time, the test chip was used to find the correct etch time for the desired depth. Using a profilometer (Dektak) the length and the width of the slit and length, width, and height of the micro channels were measured. The depth of the nanoslit is too small for the Dektak to measure accurately.

2.1.3 Patterning and etching nano-pits

The device used in chapter 4 contains pairs of nano-pits inside the slit as shown in Fig. 4.1b). Helios (ThermoFisher Scientific) focused ion beam (FIB) was used to create the nano-pits. For each pair of pits, FIB of Gallium (at 30keV ion energy) first milled a 2 μm by 5 μm trench within the slit, and then milled deeper in two square regions at both ends of the rectangle. High resolution scanning electron microscopy (SEM) on the same instrument was used to navigate the device.

Figure 4.1c) shows an SEM image of an example double pit. The square pits with width $D = 2\mu$m are separated by an obstacle with width $d = 1\mu$m. The precise dimensions of the nano-features (slit height and pits) were measured using an atomic force microscope (AFM, Asylum MFP-3D). In this technique the force experienced from the sample molecules on the probe is used to create a three-dimensional topography of the sample. Tip used for scanning was an AC160TS-R3, also knows as OTESPA, from Asylum Research by Oxford Instruments. Figure 4.1d) shows the AFM profile of the double pit.

2.1.4 Creating sealed devices with access holes

Access holes were drilled to allow insertion of fluids, electrodes, and pressure into the reservoirs, To start, two layers of S1818 photoresist was applied to both sides of the fully patterned chips to protect the chips during the drilling process. Additionally the chips were fully taped for extra protection but the reservoirs were exposed for drilling the access holes. Aluminum oxide (AlO2) powder was used to powder blast the 4 access holes (milimeter sized) through the chip at the end of each microchannel, through each reservoir. Powder blasting for 50 seconds resulted in a millimeter sized hole. After holes were drilled, the tape was removed and all the remaining photoresist and chromium was removed by standard cleaning and

chromium etchant.

Finally, each device was sealed with another silica chip (200m thick) using chip-to-chip direct method followed by thermal bonding. To start the process the patterned chips and the cover slips were sonicated in DI water, IPA, and again DI water. Next, all the chips and the cover slips were dipped in piranha (mixture of sulfuric acid and hydrogen peroxide) for 30 minutes to clean any inorganic substance that may have been left on the chips or cover-slips. The mixture consisted of H2SO4:H2O2 = 2:1 (300ml: 150ml). Next, one chip and one cover-slip were dipped in 0.5% HF for 1 minute at the same time to remove about 10 nm and smooth out the surfaces. The chip and cover slip were then rinsed in DI water and N_2 blow dried. Immediately after, the chip was moved to a hard surface and the cover slip was pushed down on the chip by a cotton swab. This process was repeated for all the chips to create 5 sealed devices. Sealed chips were annealed in a furnace in $1000°C$ for 4 hours. The temperature of the furnace was increased 4 degrees a minute to prevent cracking.

2.2 System for applying an arbitrary time-dependent pressure difference

A chuck (sample holder) was designed to hold the chip in place over the microscope. The chuck also allowed the application of pressures to the access holes, as well as electrical connection to the reservoirs. To set up an experiment, the access holes of the chips were aligned precisely with the holes in the chuck and sealed with O-rings tightly. The chuck was connected to the pressure control manifold by Luer connectors, and the manifold was connected to an automated pressure system (Fluigent) that supplies programmable air pressure. The pressure was controlled through a script software to automate the desired pressure function.

Pressure was used to drive the fluid and particles from reservoirs to microchannels and from there to the nanoslit.

2.3 System for applying an arbitrary time-dependent voltage difference

NI LabVIEW generated a white Gaussian electrokinetic noise, V(t), with an adjustable standard deviation, σ_e. We used the white Gaussian noise option that is built into the signal generation module in LabVIEW to specify the characteristic of the noise signal. The desired signal was then outputted by a NI data acquisition device (DAQ) device. White noise is a random signal with equal intensity at all frequencies and zero mean. In practice, the bandwidth of white noise is limited by different factors like our DAQ device and our transmission medium capabilities. We consider our signal to be white noise because measured voltages have mean zero and a flat spectrum over the frequency range that is relevant to the context of our experiment. We have limited this range to 0.5Hz to 50Hz, since above and below this limit is outside of the response time of the DNA. The 0 DC offset avoided transport of the DNA molecules due to a linear electric field from DC field. The generated voltage has a Gaussian distribution that goes at least up to 5 standard deviations about the mean.

The software generates a series of random numbers at a sampling rate that we determined (0.5Hz to 50Hz). The random numbers drive the voltage output of the DAQ after applying a scaling factor, σ_e, that we adjust to control the noise level, therefore each σ_e corresponds to a different noise level. After the DAQ outputted the desired voltage, an external voltage amplifier amplified the signal by a factor of 18. The amplified signal was fed back into the DAQ to perform Fourier analysis (compared the Fourier transform of the original signal with that of the amplified signal) using LabVIEW to ensure that the amplified signal still had the expected white noise characteristics after amplification.

Generated noise from the DAQ device was connected to two electrodes after the amplification and imposed across the nanoslit by immersing them in the reservoirs on either sides of the nanoslit as shown in Fig. 4.1. The electrodes were made in lab using vented screws and silver wire (Ag/AgCl) that was passed through the screw and soldered to it. The four electrodes were then screwed into the chuck, on top of the access holes of each reservoir. To ensure proper contact with the smaple, the reservoirs were fully filled.

2.4 Preparation of the nanofluidic device for an experiment

To start an experiment, the nanofluidic device was flushed with the appropriate buffer for that experiment to remove air bubbles in the microchannel and the nanoslit. Air bubbles inside the channels are easily seen through the microscope. Flushing was done by applying 400 to 500 mbar pressure to the reservoirs for up to 4 hours until no air bubbles were seen. During flushing the alignment of the O-rings were also checked, any misalignment would result in a leak visible by eye.

Next, the microscope was focused on the nanoslit and 30 μL of the sample containing fluorescent particles was added to the device through the access holes. The sample was flushed through the microchannels from one side to the other side. Since the nanoslit has a much higher resistance compared to that of the microchannels, sample required an extra force to enter the nanoslit. To push the sample inside the nanoslit from the microchannels, equal pressure (about 600 to 700 mbar) was applied from both ends of that microchannel. Any pressure imbalance would result in a drift of the particles inside the microchannels. The highest applied pressure used in my experiments was 700 mbar with a pressure resolution of 0.03% of the total pressure.

2.5 Tracking individual particles and DNA molecules

2.5.1 Fluorescence microscopy

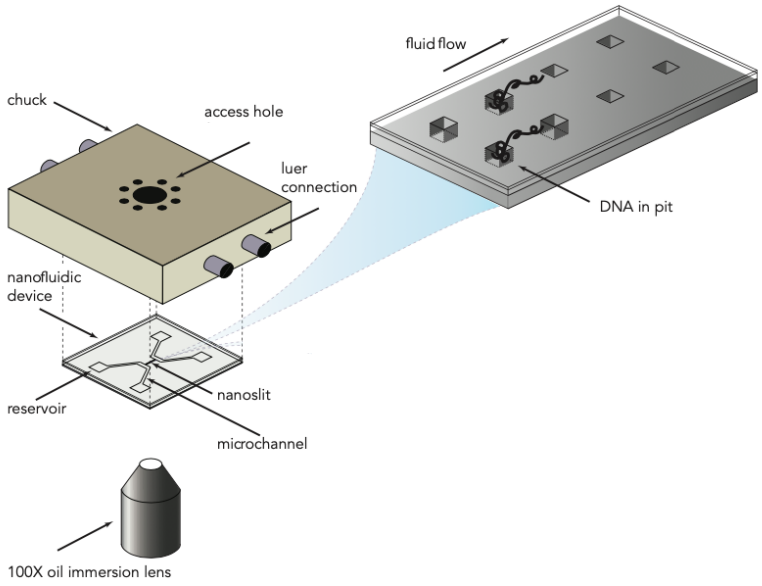

Figure 2.2: Schematic of our experimental setup, A is the chuck and B shows the slit and pit region of the nanofluidic device. Modified from [67]

The particles and molecules were tracked using fluorescent microscopy. Figure 2.2 shows an illustration of the chip assembly and the microscopy configuration where the chuck holds the fluidic device over the microscope.

The development of fluorescent microscopy has opened up new ways to capture microscopic images of polymers and sub-micron particles. The chip was illuminated by a UV light source (Illumination, EXFO). Before the UV light hit the fluidic device, it passed through a filter cube (to match the absorption wavelength of the fluorescent particle/molecule under study) that reflected the UV light onto the fluidic chip. The UV light passed through an automated shutter (Uniblitz, Vincent Associates) before reaching the fluidic chip to mini-

mize the photo-bleaching of the fluorescent particles by reducing the exposure time. Emitted fluorescent light from the particles was captured by an objective lens. Captured images were recorded with an EMCCD camera (Andor iXon) for analysis.

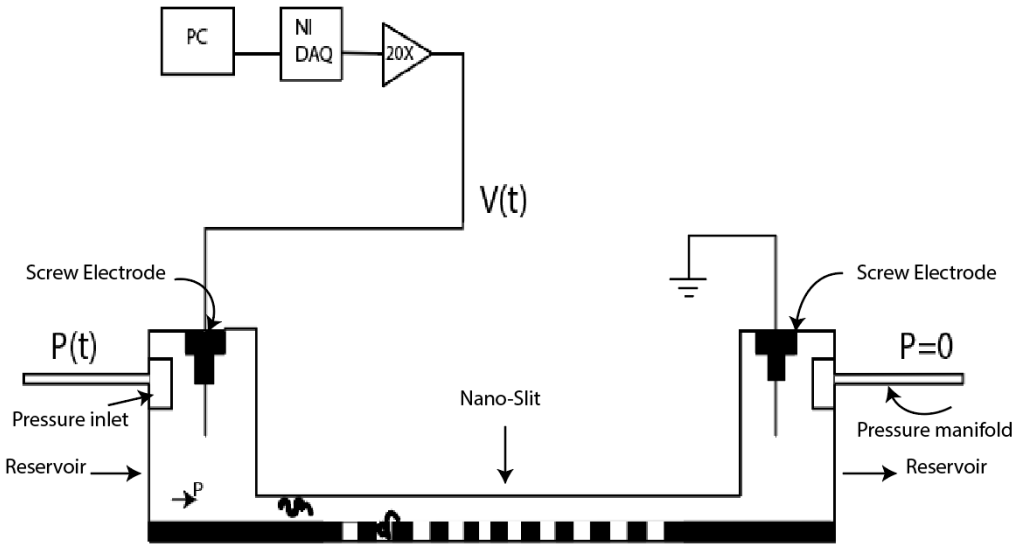

Figure 2.3: Fluidic setup showing the electrical and pressure connections.

2.5.2 Image analysis techniques

Recorded images of the particles were processed through a custom made MATLAB program that was adapted from previous lab members [67]. The original program tracks the position of the center-of-mass (COM) of the fluorescent particles and molecules from frame-to-frame by identifying the white pixels corresponding to the object from the background. Fluorescent objects appear as white pixels on a dark background in each frame. Then, the mean intensity is subtracted from each pixel to make it easier to identify fluorescent particles or molecules.

Figure 2.4 shows an example image of a fluorescent DNA molecule. The experiments in chapter 5 contain high density of particles which often cross paths. Therefore, the program

was enhanced to distinguish particles in close proximity of one another as follows: Once two particles become closer than the maximum expected step size, the program looks at the fluorescent intensity of the neighboring particles in order to match the correct particle from frame to frame. The analysis code is publicly available [68].

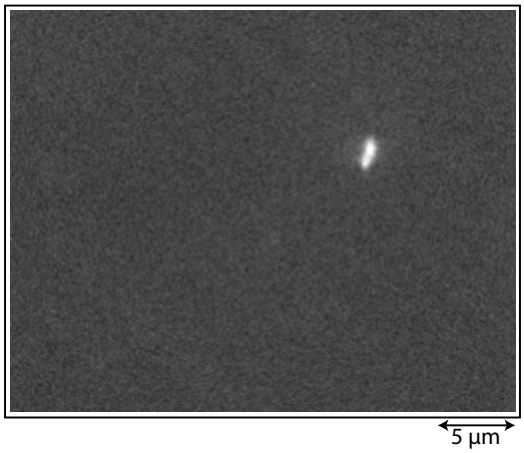

Figure 2.4: Single fluorescently stained DNA molecule inside a nanoslit

Chapter 3

Controlled Amplification of DNA Brownian Motion Using Electrokinetic Noise

3.1 Overview: DNA Brownian motion due to thermal and electrokinetic noise

As mentioned previously, having access to a large range of noise levels in fluidic devices allows one to study numerous exotic noise-driven phenomena. However, when we exclusively rely on thermal fluctuations as the source of noise, we severely restrict the noise regime in which noise-driven phenomena can be studied. In this chapter, we report a method to greatly raise the accessible noise level and amplify the Brownian motion for DNA molecules inside a nanoslits. To do so, we added an electrokinetic noise component with a noise level that we varied widely and independently of the temperature.

Figure 3.1 illustrates the experimental method. A nanoslit strongly confines DNA in the vertical dimension (z-direction) while allowing it to move freely across the relatively large slit width (x-direction) and along its length (y-direction). The motion of individual DNA

molecules is tracked in the x and y dimensions using fluorescence optical microscopy. To influence the DNA dynamics, we impose a time-dependent voltage difference, $V(t)$, across the nanoslit using electrodes immersed in liquid reservoirs at either end. $V(t)$ has similar statistical properties to thermal fluctuations, and its amplitude can be adjusted. The resulting DNA dynamics correspond to a Brownian motion with amplified fluctuations along the length of the nanoslit. Our method operates in a manner reminiscent of the anti-Brownian electrophoretic (ABEL) trap [69], except that instead of cancelling the fluctuations of suspended objects, we use electrokinetic forces to amplify them.

It is convenient to characterize the lengthwise fluctuations of DNA in our setup by an effective temperature. "Noise temperature" commonly characterizes fluctuations in electronic circuits [70]; the motion of self-propelled swimmers can be characterized by an effective temperature [71]; and in a case of particular interest to us, temperature is used to parameterize the noise strength that gives rise to stochastic resonance [12, 13]. Our nanofluidic method enables us to impose an effective temperature that is adjustable and well above the boiling point of water. By tracking individual DNA molecules and analyzing their Brownian motions, we measured their equivalent temperatures in the lengthwise direction and found it could reach 5,300 K.

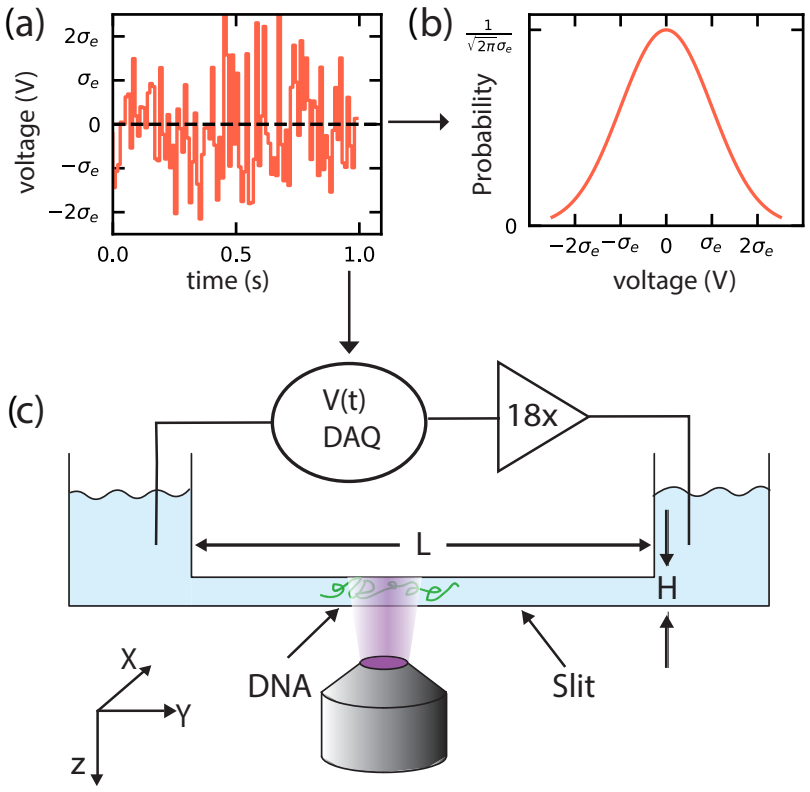

Figure 3.1: Schematic of the method for electrokinetically amplifying Brownian motion. a) A typical trace of $V(t)$. b) Gaussian distribution of voltage fluctuations. c) Illustration of the nanoslit with a fluorescently stained DNA molecule and the optical microscopy system used to track the DNA motion. The sketch indicates L, H, and the orientation of the nanoslit relative to the coordinate system.

The Brownian motion of a DNA molecule is characterized by the growth of its mean square displacement (MSD) in time,

$$\text{MSD} \equiv \left\langle (x_i(t + \Delta t) - x_i(t))^2 \right\rangle = 2D\Delta t, \tag{3.1}$$

where $x_i(t)$ is the generalized coordinate of molecule i, Δt is the time interval, $\langle ... \rangle$ denotes the ensemble average, and D is the self-diffusion constant, defined by [72]

$$D \equiv \int_0^\infty \langle \dot{x}_i(t)\dot{x}_i(0) \rangle \, dt. \tag{3.2}$$

The Brownian motion is normally driven by thermal forces alone. In that case the over-

damped Langevin equation describes the dynamics [73]

$$\dot{x}(t) = \frac{F(t)}{\zeta}, \tag{3.3}$$

where ζ is the viscous drag coefficient and $F(t)$ is a random thermal force with zero mean, i.e. $\langle F(t)\rangle = 0$ and autocorrelation $\langle F(t)F(t')\rangle = 2\zeta k_B T\delta(t-t')$ [7], where k_B is the Boltzmann constant, T is the temperature, and $\delta(t)$ is the Dirac delta function. Combining Eqs. (3.2) and (3.3) gives D_0, the thermal self-diffusivity in one dimension

$$D_0 = \frac{k_B T}{\zeta}. \tag{3.4}$$

The application of $V(t)$ across the nanoslit generates an additional electrokinetic force in the y-direction, and the corresponding Langevin equation becomes

$$\dot{y}(t) = \frac{F(t)}{\zeta} + \mu\frac{V(t)}{L}, \tag{3.5}$$

where $\mu \equiv v_{drift}/E$ is the electrophoretic mobility of the DNA, v_{drift} is the drift velocity of the particle in electric field with strength E, and $V(t)/L$ is the electric field inside the slit.

To mimic thermal noise using a signal generator with a finite bandwidth, we generate a band-limited Gaussian white noise signal for $V(t)$. This gives $\langle V(t)\rangle = 0$ and $\langle V(t)V(t')\rangle = \sigma_e^2\left(\frac{\sin(2\pi B(t-t'))}{2\pi B(t-t')}\right)$ [74,75], where σ_e is the standard deviation and B is the bandwidth. When the bandwidth of the signal generator is large compared with that of the particle tracking system, we can approximate $\langle V(t)V(t')\rangle \approx \frac{\sigma_e^2}{2B}\delta(t-t')$. $V(t)$ and $F(t)$ have similar statistical properties, but they are not correlated with each other, so $\langle F(t)V(t')\rangle = 0$. From Eqs. (3.2) and (3.5), the self-diffusion constant in the y direction is

$$D_y = D_0 + \frac{1}{4B}\left(\frac{\mu\sigma_e}{L}\right)^2. \tag{3.6}$$

Equation 3.6 predicts that the minimum DNA diffusivity is given by the thermal value, D_0, and that voltage noise increases the diffusivity in the y direction by an amount proportional to the variance of $V(t)$. From Eqs. (3.4) we can define the effective temperature of Brownian motions in the y direction, T_{eff}, to be

$$T_{\text{eff}} = T\frac{D_y}{D_0}. \tag{3.7}$$

While $V(t)$ amplifies the fluctuations of a molecule's COM, it does not affect the relative fluctuations between different segments within a molecule or between the COMs of different molecules. A voltage applied across a nanofluidic slit establishes a uniform field within it, so every segment of every molecule inside it is subjected to the same electrokinetic force at a given moment. This difference between electrokinetic noise and thermal noise can be observed in the relative diffusion between two molecules.

Fluctuations in the separation between two molecules can be parameterized by a pairwise diffusion coefficient, D^p. We obtain D^p by applying Eq. (3.5) to a pair of DNA molecules subject to the same $V(t)$. This gives $\dot{y}_2(t) - \dot{y}_1(t) = \frac{1}{\zeta}(F_2(t) - F_1(t))$ for the y direction, where $F_2(t)$ and $F_1(t)$, are the forces of thermal noise on each DNA molecule. Combining $\langle F_1(t)F_2(t)\rangle = 0$ and Eq. (3.5) we obtain

$$\langle(\dot{y}_2(t) - \dot{y}_1(t))(\dot{y}_2(t') - \dot{y}_1(t'))\rangle = \frac{4k_BT}{\zeta}\delta(t - t'). \tag{3.8}$$

From Eqs. (3.8), (3.1), and (3.2), the mean squared separation in the y direction grows in time according to

$$\left\langle[(y_2(t + \Delta t) - y_1(t + \Delta t)) - (y_2(t) - y_1(t))]^2\right\rangle = 4D_0\Delta t. \tag{3.9}$$

The separation in the x direction obeys the same relation. Therefore, $D^p = 2D_0$.

3.2 Methods

3.2.1 Preparation of fluorescently stained DNA

We used λ DNA molecules (48.5 kbp, double stranded, contour length L = 16.5 μm, 500 ug/ml New England Biolabs) that were fluorescently stained using YOYO-I dye ((491/509, 1 mM solution, Life Technologies, Thermo Fisher Scientific)) at a 10: 1 base-pair-to-dye ratio. The YOYO-1 molecules were attached into double stranded DNA molecules during an incubation at 50 °C for two hours, followed by an ice bath to secure the fluorescent molecules between the strands of the DNA. The DNA was suspended in 20 mM degassed Tris-EDTA (TE) buffer that was titrated to pH 8.0 using HCl. Next, 4% β-mercaptoethanol was added to suppress photobleaching. The DNA suspension was diluted to a final concentration of 0.2 μg/mL and slowly introduced into the nanofluidic device to reduced the number of DNA fragments.

3.2.2 Dimensions of the nanofluidic device

The fluidic device in this experiment featured a nanoslit with height $H = 110$ nm, length $L = 3.5$ mm, and width of 160 μm Fig. 3.1. The fabrication process is described in details in chapter 2. We estimate that about 80 % of the voltage applied between the reservoirs dropped across the nanoslit, based on the dimensions of the device and assuming a constant fluid conductivity.

3.2.3 DNA tracking procedure

For this project a 60× water immersion objective lens with a numerical aperture of 1.20 was used to image the DNA molecules Fig. 3.2. Images were acquired at the rate of 2 frames per second with an exposure time of 50 ms per frame. Each recording of a molecule contained 100 frames. In order to suppress possible edge effects, we only considered molecules that were at least 20 μm away from the edges of the nanoslit. 20 μm is more than 180 times

the height of the nanoslit. Consequently, hydrodynamic interactions with the nanoslit edges should be completely screened [76]. The optical microscopy system and analysis software are described in chapter 2 in detail. The raw videos of the DNA molecules analyzed in this study are publicly available [68]. Our custom-written image analysis software extracted the trajectories of individual molecules from the image sequences. The COM of each molecule was found by computing the first moment of its fluorescence intensity distribution. The analysis code is publicly available [68].

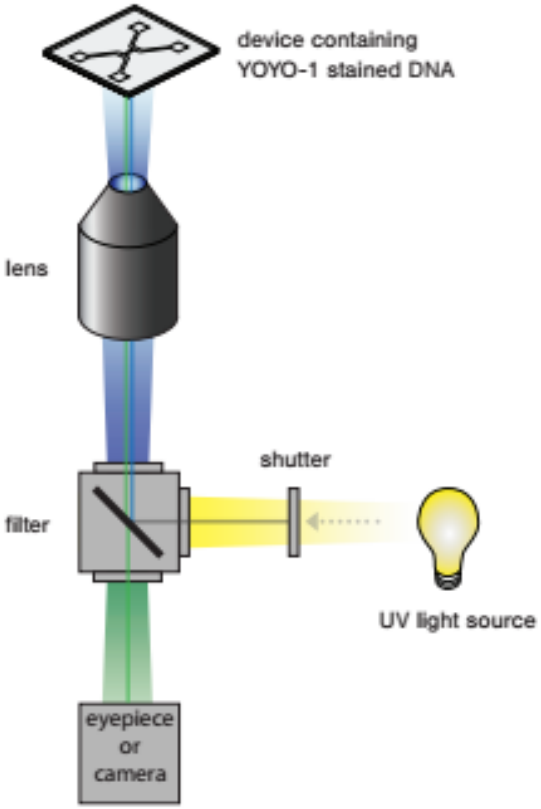

Figure 3.2: Schematic of the optical microscope setup. Adopted from [67]

3.3 Results and interpretations: DNA diffusivity as a function of the applied electrokinetic noise

The addition of voltage noise significantly increased the amplitude of the Brownian motion in the direction of the applied noise, the y direction. Figure 3.3(a) shows a sequence of images of a fluorescently labeled λ DNA molecule inside a nanoslit moving under the influence of thermal forces alone. The COM of the molecule moved only about 2 μm in the x and y directions in 40 s (although the DNA configuration changed noticeably in that time). Figure 3.3(b) shows a similar sequence of images, except in this case diffusion was assisted by an applied voltage noise with $\sigma_e = 36$ V. The COM moved about 15 μm in the y direction and about 2 μm in the x direction in 40 s. Figure 3.3(c) compares the trajectories of a selection of DNA molecules moving with and without added $\sigma_e = 36$ V electrical noise, clearly showing that the added electrical noise amplified the fluctuations. Figure 3.3(d) compares the dependence of MSD on Δt for molecules experiencing only thermal noise with the dependence for molecules subjected to a noise level of $\sigma_e = 36$ V. We obtained D_x and D_y by fitting Eq. 3.1 to the slopes of the data. In the case of pure thermal diffusion ($\sigma_e = 0$), the diffusion coefficients were $D_x = 0.130 \pm 0.006$ μm^{2}s^{-1} in the x direction and $D_y = 0.137 \pm 0.005$ μm^{2}s^{-1} in the y direction. With the addition of $\sigma_e = 36$ V noise, the diffusion coefficient in the y direction increased by a factor of approximately 19 (to $D_y = 2.5 \pm 0.3$ μm^{2}s^{-1}), but the diffusion coefficient in the x direction ($D_x = 0.21 \pm 0.07$ μm^{2}s^{-1}) was not significantly altered.

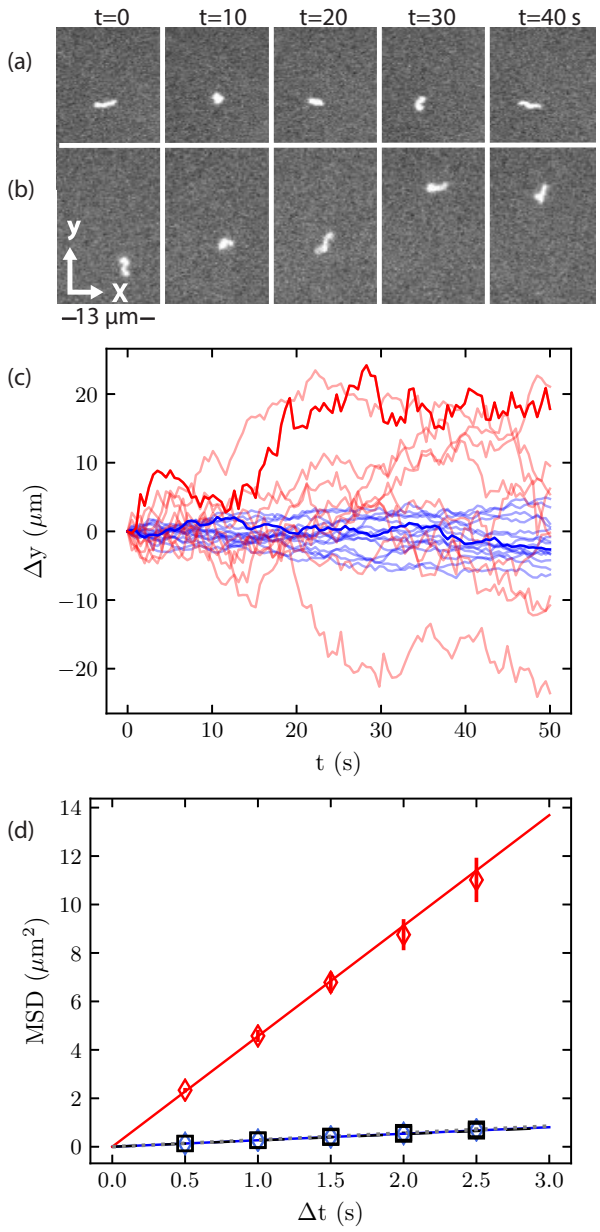

Figure 3.3: (a) Time-resliced images of a fluorescently labeled λ DNA molecule diffusing in TE buffer with no voltage noise and (b) with a voltage noise level of $\sigma_e = 36\,\mathrm{V}$. (c) λ DNA trajectories in the y direction with no applied noise (blue) and an applied noise level of $\sigma_e = 36\,\mathrm{V}$ (red). The two bold lines correspond to the molecules shown in (a) and (b). (d) Dependence of the MSD on Δt, with diamonds indicating the y direction and squares the x direction. Blue symbols indicate no applied noise and red symbols a noise level of $\sigma_e = 36\,\mathrm{V}$. Lines are linear fits to the data. The lines for y-motion with no added noise (solid), x-motion with no added noise (dotted), and x motion with $\sigma_e = 36\,\mathrm{V}$ (dashed) all overlap. All measurements were performed in the same $H = 110\,\mathrm{nm}$ slit. Error bars represent one standard deviation.

We studied 50 - 70 DNA molecules for each of the 8 different values of σ_e tested. Figure 3.4 shows the dependence of the mean D on σ_e^2 for both the x and y directions. D_y increased linearly with σ_e^2, while D_x was relatively insensitive to σ_e. Based on Eq. (3.6), we fit the function $D = D_0 + \alpha\sigma_e^2$ to the measured data in Fig. 3.4, using D_0 and α as fitting parameters. In the x direction the fit obtained $D_{0,x} = 0.130 \pm 0.003$ $\mu\text{m}^2\text{s}^{-1}$ and $\alpha_x = (0.014 \pm 0.007) \times 10^{-3}$ $\mu\text{m}^2\text{s}^{-1}\text{V}^{-2}$; the small increase of D_x with noise level is not predicted by Eq. (3.4), but could have been caused either by inhomogeneities in the channel that give rise to lateral (x direction) electric field components or a slight misalignment of the fluidic channel relative to rows and columns of camera pixels. In the y direction the fit obtained $D_{0,y} = 0.139 \pm 0.005$ $\mu\text{m}^2\text{s}^{-1}$ and $\alpha = 1.82 \pm 0.06 \times 10^{-3}$ $\mu\text{m}^2\text{s}^{-1}\text{V}^{-2}$. The values of $D_{0,y}$ and D_0, which were measured independently, are the same within experimental error; this was predicted by Eq. 3.6. The measured value of α enables us, through $\alpha = \mu^2/(4BL^2)$ from Eq. 3.6, to find the DNA mobility inside the nanoslit: We found $\mu = (2.11 \pm 0.16) \times 10^4$ $\mu\text{m}^2\text{s}^{-1}\text{V}^{-1}$. That value includes contributions from DNA's electrophoresis through the fluid and the electroosmotic flow of fluid within the channel. We note that it is similar in magnitude to the free electrophoretic mobility of double-stranded DNA in Tris-borate-EDTA buffer, 4.5×10^4 $\mu\text{m}^2\text{s}^{-1}\text{V}^{-1}$ [77].

The enhancement of DNA fluctuations in the y direction can be interpreted as an increase in the effective temperature caused by $V(t)$. We calculated T_{eff} using Eq. (3.7), with $T_0 = 298 \pm 2$ K being the true thermal temperature. T_{eff} increased linearly with σ_e^2 and reached a maximum of 5,300 K at the highest noise level, $\sigma_e = 36$ V (Fig.3.4). However, unlike thermal noise, the voltage noise causes correlated fluctuations of different molecules and their segments. This technique unlocks a previously inaccessible effective temperature regime for studies and applications of noise-dependent phenomena.

We investigated the spatial correlations of electrokinetic noise by measuring the relative displacements of pairs of DNA molecules subjected to the same $V(t)$ with $\sigma_e = 18$ V. Figure 3.5 plots the growth in the mean square distance between the centers of mass, in both

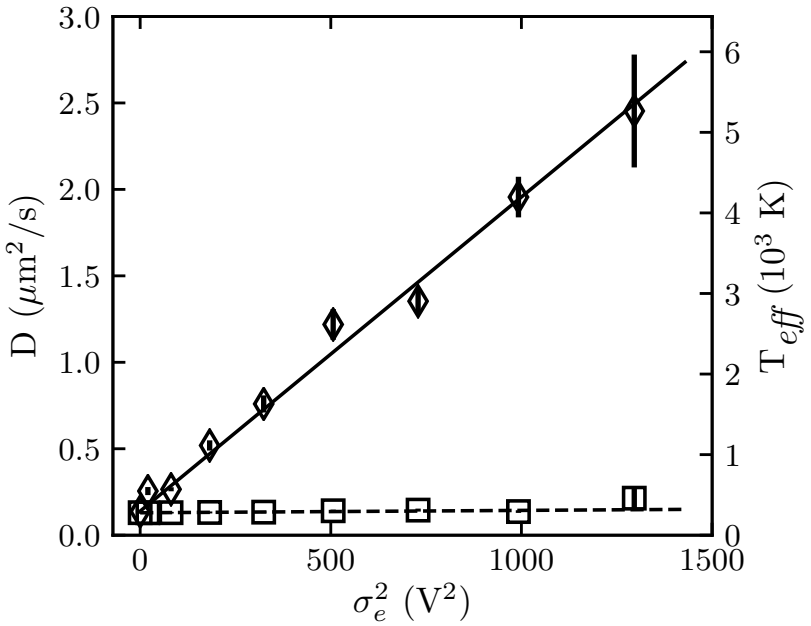

Figure 3.4: Dependence of D on σ_e in the x (squares) and y (diamonds) directions. Lines are linear fits using $D = D_0 + \alpha\sigma_e^2$. Right axis indicates the corresponding effective temperature. Error bars are the standard error from a bootstrap analysis of 1000 re-samplings of diffusion coefficients of DNA molecules.

the x and y directions, for 20 such pairs. The MSD for the pairs increased linearly with time, with very similar slopes for the x and y directions. The slopes reflect pairwise diffusion coefficients, D^p. Using Eq. 3.1, we found $D_x^p = 0.25 \pm 0.01$ μm^{2}s^{-1} and $D_y^p = 0.26 \pm 0.01 \mu m^2 s^{-1}$ in the x and y directions, respectively. Those values are almost exactly double the thermal diffusion coefficient of a single molecule in one dimension, $D_0 = (0.13 \pm 0.01)$ μm^{2}s^{-1}, which we obtained from the trajectories of the same molecules analyzed individually.

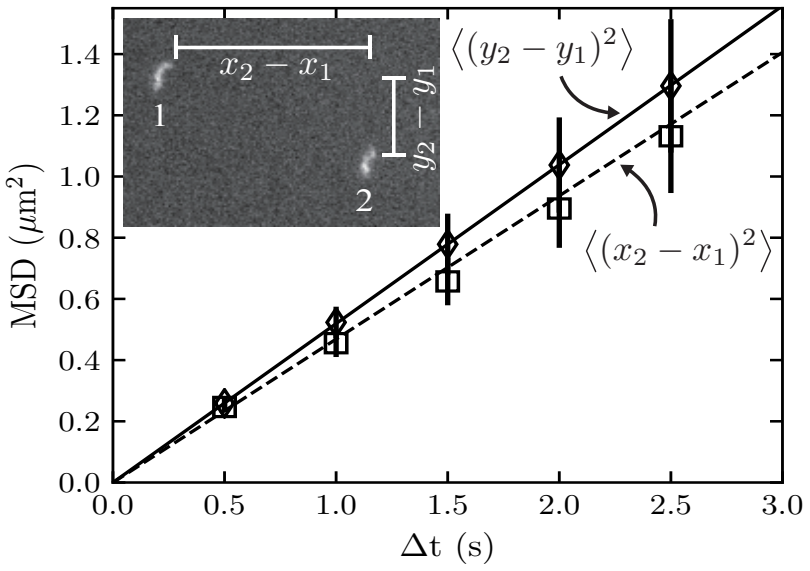

Figure 3.5: The mean-squared separation between two λ DNA molecules subjected to the same $\sigma_e = 18$ V voltage noise is plotted as a function of time for the x (squares) and y (diamonds) directions. Lines are linear fits to the x (dashed) and y (solid) data.

The spatially correlated nature of electrokinetic forces explains why a double-stranded DNA molecule can survive much higher effective temperatures than thermal temperatures. No tension, compression, or shear builds up in the molecule as the result of electrokinetic noise. Thermal forces, on the other hand, are applied in random directions to different parts of a molecule. The resulting stresses must be balanced by internal molecular binding forces, and a molecule loses its ability to do that above the melting temperature.

Figure 3.6 shows the dependence of the DNA radius of gyration, R_g, on σ_e. R_g was obtained from analyses of the molecular fluorescence intensity distributions, as described in Ref. [63]. R_g was relatively insensitive to σ_e: The mean value was 1.04 ± 0.01 μm, and a linear fit found that R_g increased by only 5% of its initial value over the full range of σ_e. These observations lead us to conclude that the observed changes in diffusivity with σ_e are not caused by changes in the hydrodynamic radius of the DNA.

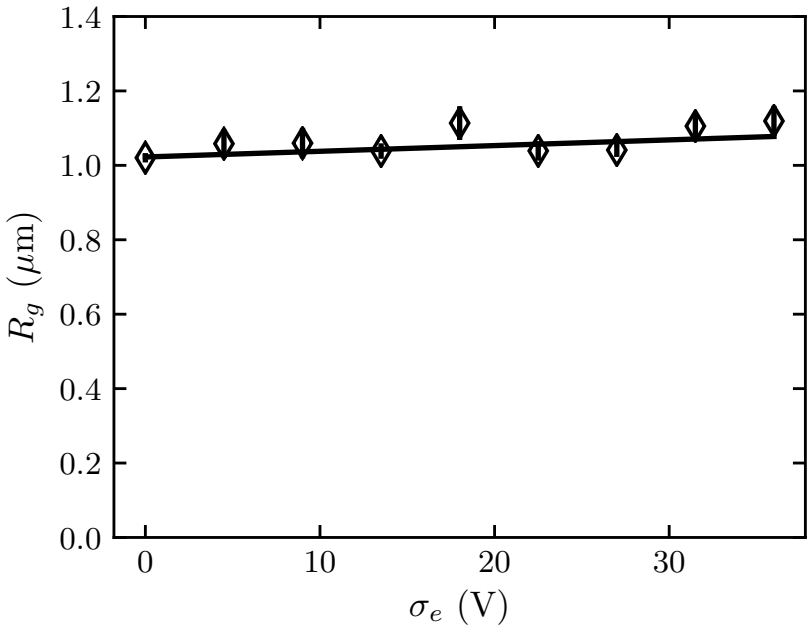

Figure 3.6: Dependence of R_g on σ_e. Each point is the mean R_g of the λ DNA molecules measured for each σ_e; the same molecules were analyzed in Fig. 3.4. The line is a linear fit.

3.4 Concluding remarks

The technique described here opens up new possibilities for studying noise-driven phenomena in previously inaccessible regime. For example stochastic resonance which is a noise-driven phenomenon could be studied in new ways with electrokinetic noise. SR involves a nonlinear system whose response to a weak periodic signal obtains a maximum for some optimum noise level [14, 15, 78]. In a nanofluidic experiment involving DNA, the hallmark of SR would be a maximum in the synchronization between a weak periodic driving force and the hopping of a DNA molecule back and forth between two nano-pits as a function of T_{eff}. To observe that in practice, one needs to vary the noise level over an extremely wide range and independently of the barrier between pits. An ability to raise T_{eff} to otherwise impossible levels also raises the possibility of studying nonequilibrium dynamical phenomena, which have attracted growing interest recently [79–84].

Additionally, Kramers' kinetics can be studied in a new regime. The starting point for

Kramers' theoretical model of reaction rates is a Langevin equation with an energy landscape featuring a barrier and a white Gaussian noise term whose delta-correlated amplitude characterizes the temperature [10]. DNA dynamics consists of energy landscape term(s), and a noise term. The same model describes the dynamics of DNA in our experiments, except the noise term in Eq. 3.5 combines electrokinetic and thermal forces, which are uncorrelated but have the same statistical properties. Thus, like Kramers' model, Eq. 3.5 obtains the familiar Arrhenius kinetics, but with an effective temperature defined by Eq. 3.7.

In the next chapter we show that in a nanoslit with an embedded nanotopography, long DNA molecules become trapped inside nano-pits where their configuration entropy is relatively high, and to hop to a neighboring pit, the molecule must overcome an entropic barrier in the free energy landscape [62–64]. Raising T does not significantly increase the hopping rate in this system because the entropic barrier, which results from thermal fluctuations of segments within a molecule, also grows in proportion with T. But our electrokinetic technique grants us control over the fluctuations in a polymer's center of mass independently of the thermal fluctuations of its segments. Raising T_{eff} leaves the entropic barrier unchanged and enable us to manipulate the hopping rate over a wide and interesting range.

Chapter 4

Noise Assisted Barrier Crossing of DNA Molecules in a Nanofluidic Environment

4.1 Overview: from Kramer's reaction rate theory to DNA barrier hopping.

Nearly 100 years have passed since Kramers started work on reaction-rates [8] that led to a general theory of barrier crossing processes [9]. Kramers' theory now serves as a model for phenomena ranging from chemical reactions [10], to major shifts of Earth's climate [78,85,86], to crashes in the stock market [87, 88]. The theory relates the noise in a system (i.e., its intrinsic fluctuations) to the rate K that the system overcomes an energetic barrier. Barrier crossing phenomena in fluidic environments, including molecular sieving [61, 89, 90], giant acceleration of diffusion [91–93], and escape of trapped molecules from confinement [56, 94–96]. Such phenomena are interesting and potentially technologically useful are normally driven by fundamental thermal fluctuations. Kramers' theory, which applies equally well to non-thermal noise sources, illuminates ways on increasing the noise range independently of

temperature.

We reported a method in chapter 3 for injecting a controllable level of electrokinetic noise into a fluidic device and thereby amplify the Brownian motion of DNA polymers [97]. Here, we use this technique to control the rate of DNA hopping over an entropic barrier in a nanofluidic device. We also present a numerical model of the DNA hopping between two neighboring pits. The model accounts for the shape and extent of the free energy landscape compared to that of Kramers'.

4.2 Experimental setup: characteristics of the bistable entropic trap and the applied electrokinetic noise

Figure 4.1b illustrates a device with two neighboring nano-pits that creates a free energy landscape for DNA with two entropic traps. The free energy of DNA is relatively low inside a nano-pit because it can explore more configurations and increase its configurational entropy there. The height of the free energy barrier between the nano-pits is determined by the confining dimensions, in particular the height of the constriction separating the nano-pits [64, 98].

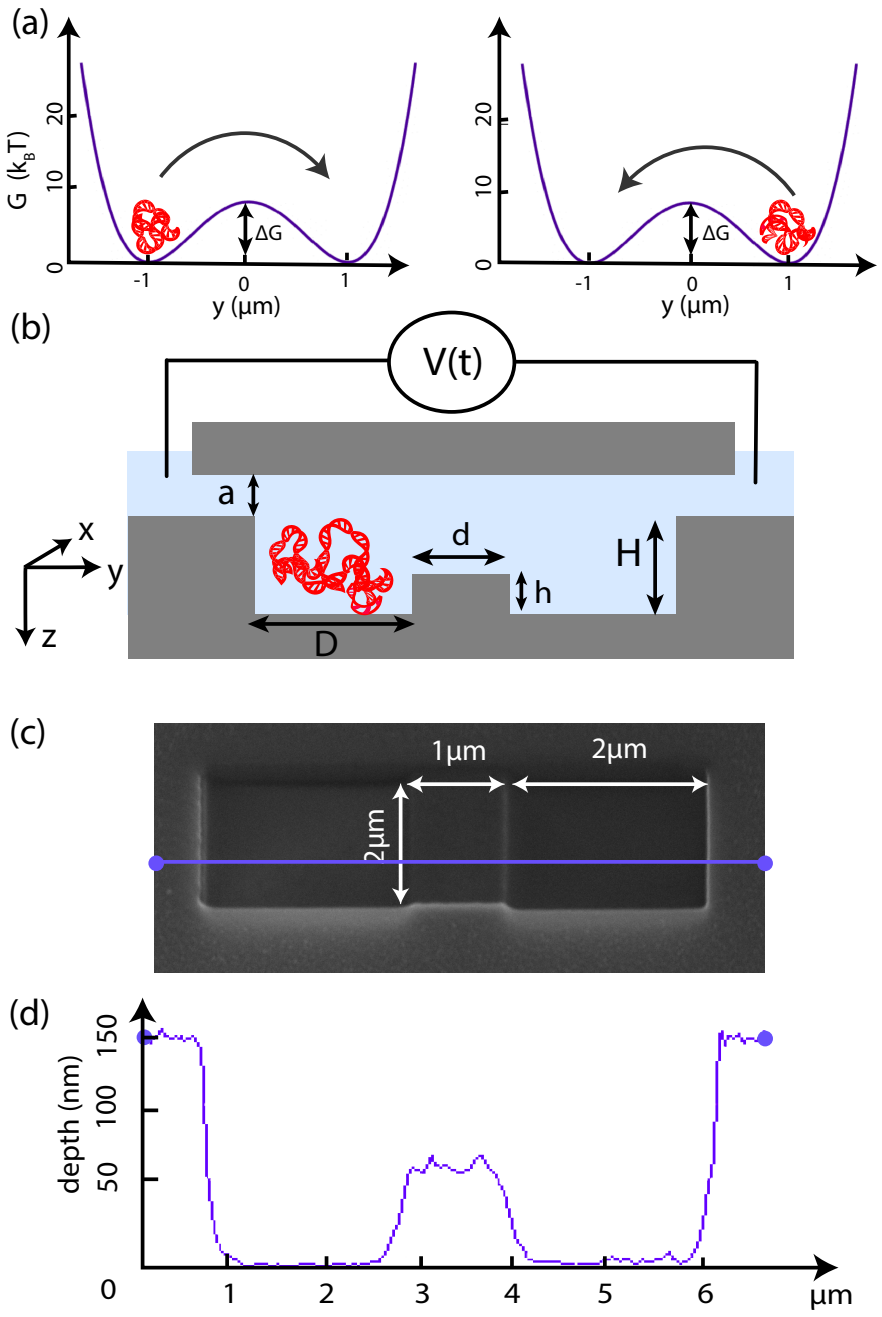

Figure 4.1: Noise-assisted hopping. a) Schematic of DNA hopping between two free energy minima separated by a barrier of height $\Delta G^{\dagger}$. b) Nanofluidic device cross section with two nano-pits that create entropic traps for a DNA molecule. The sketch shows the voltage noise source and the dimensions H, h, D, d, and a. c) Scanning electron micrograph of nano-pits viewed from above. d) Height profile measured across a pair of nano-pits as indicated by the blue line in c).

A nanofluidic device was fabricated on a glass chip with a nanoslit of height $a = 75$ nm,

length $L = 3.5$ mm, and width of 160 μm (Fig. 4.1b). Two U-shaped microchannels, each 0.5 μm deep, connected the nanoslit to two pairs of reservoirs. The device was made using methods described in chapter 2. The pits are $H = 150$ nm deep and the obstacle between them rises a height $h = 50$ nm above that. The purpose of the raised obstacle was to create an entropic barrier in the free energy landscape for confined DNA that molecules needed to overcome in order to move to the neighboring pit. A surface roughness with a peak-to-peak range of approximately 10 nm, as measured by atomic force microscopy, is the main source of experimental uncertainty in theoretical estimates of the free energy barrier; we parametrize the uncertainty in h and H with the 3.5 nm RMS roughness.

Chapter 2 and 3 described the generation and application of the electrokinetic noise across a nanoslit. Briefly, a digital-to-analog voltage controller applied a time-dependent noise voltage $V(t)$ across the nanoslit. $V(t)$ had Gaussian fluctuations with an adjustable standard deviation, σ_e, zero mean, and a finite bandwidth ΔB. The resulting electric field induced a fluctuating force on confined molecules, as illustrated in Fig. 4.1 b. The applied voltage is related to the resulting DNA velocity by the electrophoretic mobility, $\mu = v/E(t)$, which accounts for the electrophoretic DNA motion through the fluid and the electro-osmotic flow of fluid within the channel.

4.3 Simulations of a Brownian particle in a bistable potential

To get a better insight into shorter and longer timescales, we simulated a point particle in a bistable potential with a fixed energy barrier, as illustrated in Fig. 4.1 a. The dynamics are described by a Langevin equation for an overdamped Brownian particle at position y

$$\dot{y} = -\frac{dG(y)}{dy}\frac{1}{\zeta} + \sqrt{\frac{2D_{\text{eff}}}{dt}}dW_t, \tag{4.1}$$

where D_{eff} is the effective diffusion coefficient under σ_e, ζ is the drag coefficient, and W_t is a standard Wiener process with $\langle dW_t^2 \rangle = dt$. As we reported previously [97], D_{eff} is related to σ_e^2 and the thermal diffusivity, D_0, by $D_{\text{eff}} = D_0 + \alpha\sigma_e^2$. D_0 depends on the confinement of the nanofluidic device. However, D_0 is expected to vary only modestly between the different parts of the double-pit structure: When a molecule is above the central barrier, the effective slit height is 175 nm and $D_0 \approx 0.08\ \mu m^2/s$, and when the molecule is in either pit, the effective slit height is 225 nm and $D_0 \approx 0.11\ \mu m^2/s$. For the purpose of simplifying our numerical model calculations, we implemented a uniform diffusivity.

The value $D_0 \approx 0.09\ \mu m^2/s$ we used corresponds to the diffusivity of λ DNA in a slit of intermediate height $H = 200$ nm, based on its bulk radius of gyration $Rg = 0.69\ \mu$m, its bulk self-diffusion coefficient $D_{\text{bulk}} = 0.46\ \mu$m/s [99], and the previously measured relationship between D_0, D_{bulk}, R_g, and H for DNA confined in a nanoslit [100]. It is reasonable to base estimates of DNA diffusivity in our device on theory and measurements of DNA in slits, because the in-plane radius of gyration for λ DNA confined in a 200 nm deep slit is about 0.7 μm [101], hence a molecule at the center of a $2\ \mu m \times 2\ \mu m$ square pit should not significantly interact with the pit edges. The double-well potential $\Delta G(y) = -c_2 y^2 + c_4 y^4$ is sketched in Fig. 4.1a. The parameters $c_2 = 12.2\ k_BT(\mu\text{m})^{-2}$ and $c_4 = 6.1\ K_BT\ (\mu\text{m})^{-4}$ describe a free energy landscape with a barrier of height $\Delta G^\dagger = 6.2 \pm 0.4\ k_BT$ between the two minima.

The parameters were obtained by another group member, Tim Zhao from a theoretical scaling model of the confinement free energy [63, 98, 102, 103]. Previous studies have shown that Flory scaling theory gives a good description of long DNA polymers inside nanofluidic structure like ours [63, 98]. The free energy for a polymer of persistence length P (≈ 50 nm for dsDNA) and effective thickness w (≈ 10 nm for dsDNA) in a rectangular pit of dimensions x_1, x_2, and x_3, ΔG_{pit}, is given by [102]

$$\frac{\Delta G_{\text{pit}}}{k_BT} \approx Al_p + Bl_p^2, \tag{4.2}$$

where l_p is the length of the polymer inside the pit, $A = P(x_1^{-2} + x_2^{-2} + x_3^{-2})$, and $B = w(x_1x_2x_3)^{-1}$. The first term of Eq. 4.2 describes the confinement free energy of an ideal chain in the pit, while the second term accounts for the free energy of excluded-volume interactions between DNA segments in the same pit. For λ DNA in our nanofluidic device, the second term is an order of magnitude smaller than the first term, so we drop it and model DNA polymers as ideal chains moving forward.

To hop to a neighboring pit, a DNA molecule must first extend enough of its contour length over the obstacle to reach the neighboring pit. That extended length of the polymer inside the slit, l_s, experiences increased vertical confinement and stretching, both of which increase its free energy. The additional spring free energy of the stretched l_s scales as [63,103]

$$\frac{\Delta G_{\text{spring}}}{k_BT} \approx \frac{C}{l_s}, \tag{4.3}$$

where $C = 3d^2/4P$, and d is the distance between pits.

The total free energy of a DNA as it hops over the barrier has four components: The spring free energy ΔG_{spring} of the segment stretched between the two pits, and the confinement free energies ΔG_{p1}, ΔG_{p2}, and ΔG_{ps}, of the lengths l_{p1}, l_{p2}, and l_s of DNA that reside, respectively, in the first pit, in the second pit, and over the obstacle between them [63, 98]. The prefactors A_p and A_s are calculated using the dimensions of the pits and slit, respectively. The fixed contour length of a λ DNA molecule, $L = 16.5$ μm, constrains the partitioning of DNA contour within a nanofluidic device as $L = l_{p1} + l_{p2} + l_s$.

The activation barrier for hopping, $\Delta G^{\dagger}$, is the minimum increase in free energy that enables the DNA to reach the opposite pit and transfer its contour into it. As has been previously shown [63] and according to Eqs. 4.2 and 4.3, extending a segment of length l_s across the obstacle raises the free energy of the DNA by

$$\frac{\Delta G}{k_BT} \approx (A_s - A_p)l_s + \frac{C}{l_s}, \tag{4.4}$$

which has minimum value of $\Delta G^{\dagger} \approx 2\sqrt{(A_s - A_p)C}$. Equation 4.4 predicts that $\Delta G^{\dagger}$ is independent of P and the DNA contour length; it only depends on the physical dimensions of the nanofluidic device. Based on the dimensions of our device, we obtain $\Delta G^{\dagger} \approx 6.1\ k_B T \mp 0.4$. The uncertainty in $\Delta G^{\dagger}$ was calculated based on the $\pm 3.5\ nm$ RMS roughness of the slit.

The minima of the free energy landscape are located at $y = \pm 1\ \mu$m, which is where we estimate the λ DNA coil begins to interact with the physical obstacle. We simulated trajectories by solving Eq. 4.1 using Euler's method in Python with a time step of $dt = 1$ ms.

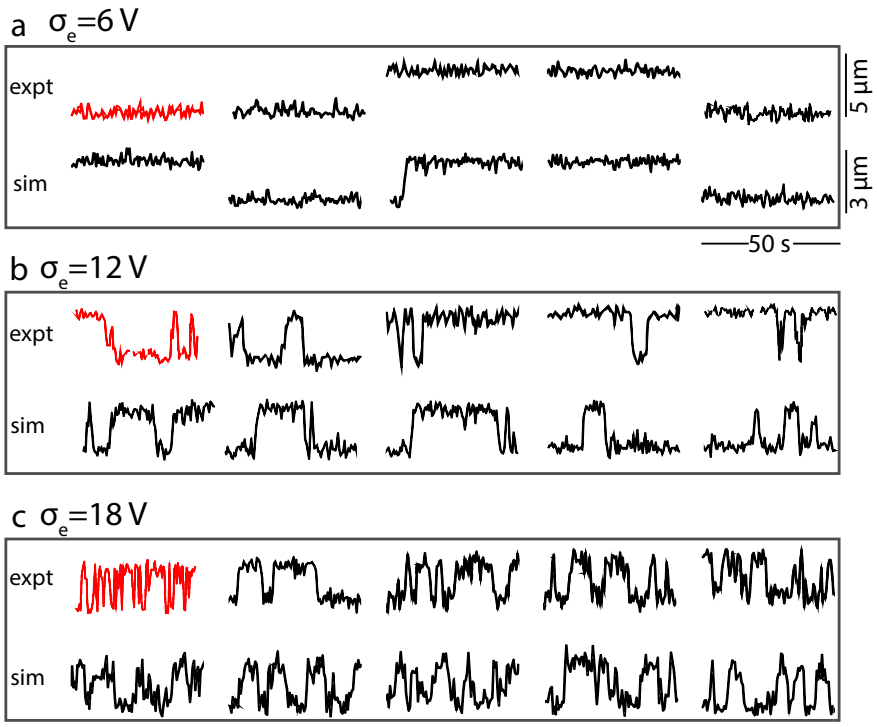

Figure 4.2: Representative trajectories of DNA molecules in the y direction are presented from measurements and simulations with a) $\sigma_e = 6\ V$, b) $\sigma_e = 12\ V$, and c) $\sigma_e = 18\ V$. Vertical scale bars are 5 μm for experimental traces and 3 μm for simulations. Horizontal scale bars are 50 s. The red trajectories correspond to the molecules represented in Fig 4.3. Simulated trajectories were sampled every $\Delta t = 500\ ms$, matching the experiments.

Figure 4.6 compares experimental and simulated DNA trajectories over 50 s intervals at different σ_e. Custom image analysis software [63, 93, 97] obtained the DNA center-of-mass

(COM) location every $\Delta t = 500$ ms from the video recordings. The simulated trajectories presented in Fig. 4.6 were also sampled every $\Delta t = 500$ ms, although the trajectories were computed using a time step of $dt = 1$ ms. The measured and simulated trajectories corresponding to the same noise intensity are both qualitatively and quantitatively similar, with the understanding that an exact correspondence of stochastic trajectories is not to expected: With $\sigma_e = 6$ V, none of the 5 measured DNA trajectories showed a hop, while only a single hop occurred within the 5 simulated trajectories. As σ_e increased to 12 V, the frequency of hops increased to about 5 per 50 s interval for both the measured and the simulated trajectories. At $\sigma_e = 18$ V, the hops occurred so frequently in both measurements and simulations that it became difficult to distinguish individual hops by eye.

To systematize our analysis of noise-assisted hopping, we define a hop by the following rule: A successful hop occurs when the COM escapes the boundary of one pit and subsequently enters the boundary of the neighbouring pit. The relevant boundaries are illustrated as yellow dashed lines in Fig. 4.3a.

4.4 Results: DNA hopping rate as a function of the applied electrokinetic noise

The experimental and numerical methods reported here significantly expand the range of noise levels and timescales over which activated DNA hopping processes can be controlled and investigated.

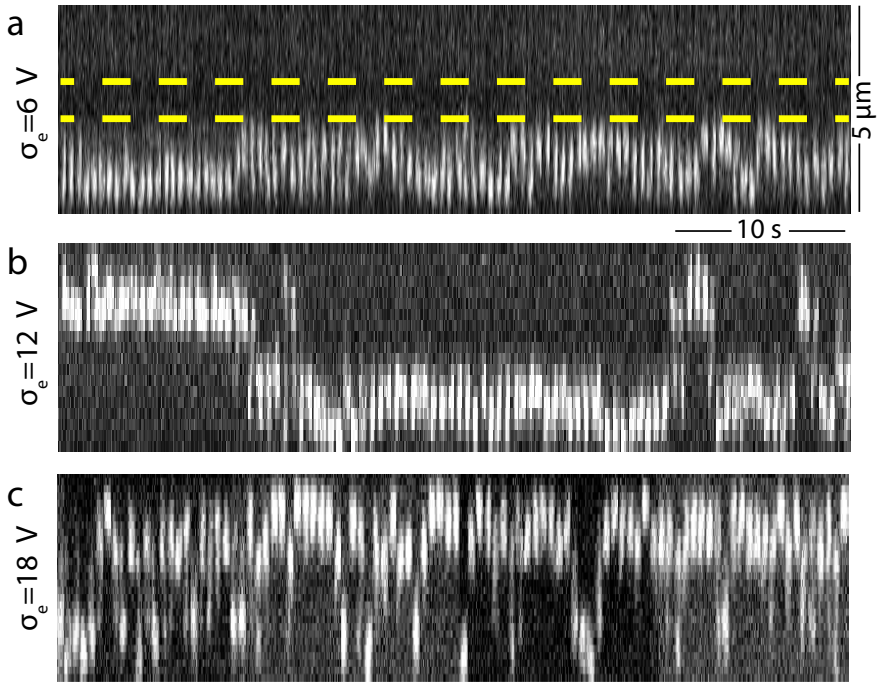

Figure 4.3: Montage of time-resliced fluorescence images of a λ-DNA molecule hopping between neighboring nano-pits with (a) $\sigma_e = 6$ V, (b) $\sigma_e = 12$ V, and (c) $\sigma_e = 18$ V applied across the fluidic device. (a) shows the boundaries between the pits and the central obstacle. The outer boundaries of the pits reach the upper and lower boundaries of the image. The contrast and brightness of the images were adjusted for clarity.

Figure 4.3 shows representative λ DNA trajectories under the influence of different levels of applied noise. With a low noise level of $\sigma_e = 6$ V, a molecule remained trapped within a single pit for the 50 s duration of the measurement (Fig. 4.3a). With $\sigma_e = 12$ V, an identical molecule hopped between the two pits about 7 times in total, with apparently random intervals of time between each hop (Fig. 4.3b). $\sigma_e = 18$ V resulted in about 20 hops in the same time interval (Fig. 4.3c). We note that we only tracked molecules that were at least 20 μm away from the edges of the 160 μm slit in order to avoid possible edge effects.

The data in Fig. 4.3b shows that the DNA molecule occasionally straddled two pits simultaneously for more than a single frame of the video. This indicates that DNA could require more time than the 0.5 s interval between images to overcome the central obstacle, especially for low values of σ_e. We also note that in Fig. 4.3c the molecule occasionally hops

back and forth between the two pits with every frame. This suggests that the crossing time may be significantly shorter than the 0.5 s interval between frames when σ_e is large. Taken together, the observations emphasize that in our measurements the DNA cannot move the distance between pits instantaneously, nor can the camera resolve the fastest crossing rates. To build a theoretical understanding of the dynamics, we developed a numerical model that takes these important physical factors into account.

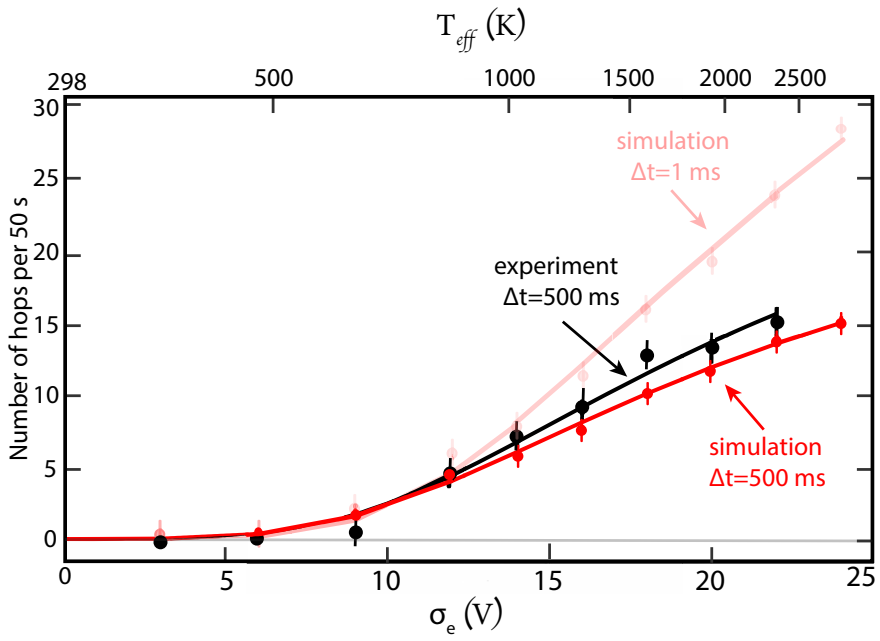

Figure 4.4: σ_e-dependence of the mean number of DNA hops between nano-pits in a 50 s interval. Black dots are mean experimental hops from at least 40 DNA molecules. Dark red dots represent mean hops from 100 simulated trajectories sampled at $\Delta t = 500$ ms. Light red dots are mean hops from the same simulated trajectories but sampled at $\Delta t = 1$ ms. Error bars are the standard error. Solid curves are fits of Eq. 4.6 to the data, obtaining $K_0 = 0.64\ s^{-1}$ and $\Delta G^\dagger = 7.7\ k_BT$ for the experiments, $K_0 = 0.54\ s^{-1}$ and $\Delta G^\dagger = 7.4\ k_BT$ for the simulations with $\Delta t = 500$ ms, and $K_0 = 1.23\ s^{-1}$ and $\Delta G^\dagger = 10.1\ k_BT$ for the simulations with $\Delta t = 1$ ms.

Figure 4.4 shows relationships between the hopping rate and σ_e. In measurements, DNA molecules were stably pinned in one pit or the other for low values of σ_e. The hopping rate increased rapidly from 0.01 s^{-1} to 0.26 s^{-1} as σ_e increased from 9 V to 18 V, beyond which value the hopping rate began to saturate. The results from the simulated trajectories closely

followed the measured results when the sampling rates matched ($\Delta t = 500$ ms). However, when the same simulated trajectories were sampled every $\Delta t = 1$ ms, the number of hops detected increased more rapidly beyond $\sigma_e = 9$ V; the hopping rate reached 0.47 s^{-1} at $\sigma_e = 22$ V, as compared with 0.27 s^{-1} with $\Delta t = 500$ ms. An explanation for this discrepancy is that some back-and-forth hops that complete in less than 500 ms are undetectable in trajectories sampled at $\Delta t = 500$ ms, whereas they can be observed with $\Delta t = 1$ ms. The discrepancy is low at low σ_e because rapid hops are less likely to occur.

4.5 Discussions: shortcomings of the Arrhenius model in describing the DNA hopping rate over an entropic trap.

The σ_e-dependent hopping rate seen in Fig. 4.4 is reminiscent of a thermally activated barrier crossing process, except in this case, electrokinetic noise plays the role of temperature. We previously reported how the addition of electrokinetic noise across a nanoslit amplifies Brownian dynamics in a way that can be characterized by an effective temperature [97]

$$T_{\text{eff}} = T(1 + \alpha\sigma_e^2). \tag{4.5}$$

Combining Eq. 4.5 with the Arrhenius equation obtains a simple model of the noise-assisted hopping rate

$$K = K_0 \exp\left[-\frac{\Delta G^\dagger}{k_B T(1 + \alpha\sigma_e^2)} \right], \tag{4.6}$$

where K_0 is the attempt rate and $\Delta G^\dagger$ is the barrier height. We fit Eq. 4.6 to the data in Fig. 4.4, using K_0 and $\Delta G^\dagger$ as fit parameters. The Arrhenius rate and the DNA hopping rate both rise rapidly beyond a certain effective temperature threshold. The fits follow each data set closely, and the measured and simulated trajectories with $\Delta t = 500$ ms obtained

comparable values for K_0 and $\Delta G^{\dagger}$.

Shortcomings of the simple Arrhenius model are revealed by fits of Eq. 4.6 to the data in Fig. 4.4. Consider the simulated trajectories: Whereas the true barrier height was $\Delta G\dagger = 6.1 k_B T$, the fit of Eq. 4.6 obtained a somewhat higher value, $\Delta G\dagger = 7.4 k_B T$, for $\Delta t = 500$ ms, and a significantly higher value, $\Delta G\dagger = 10.1 k_B T$, for $\Delta t = 1$ ms. Furthermore, the fit value of K_0 was inconsistent; the value obtained with $\Delta t = 500$ ms was less than half the value obtained with $\Delta t = 1$ ms. Why does the Arrhenius model fall short? The model only considers a fixed free energy barrier between two stable states, without accounting for the distance between them or the time it takes an object to travel that distance. That approximation is reasonable for low σ_e, where the DNA molecule is strongly confined and spends most of the time inside a pit. However, for high σ_e the DNA molecule hops frequently across the free energy landscape, and the time it spends in transit between the pits becomes a significant fraction of the total time. A model must account for the finite distance between the free energy minima to accurately describe the dynamics at high σ_e.

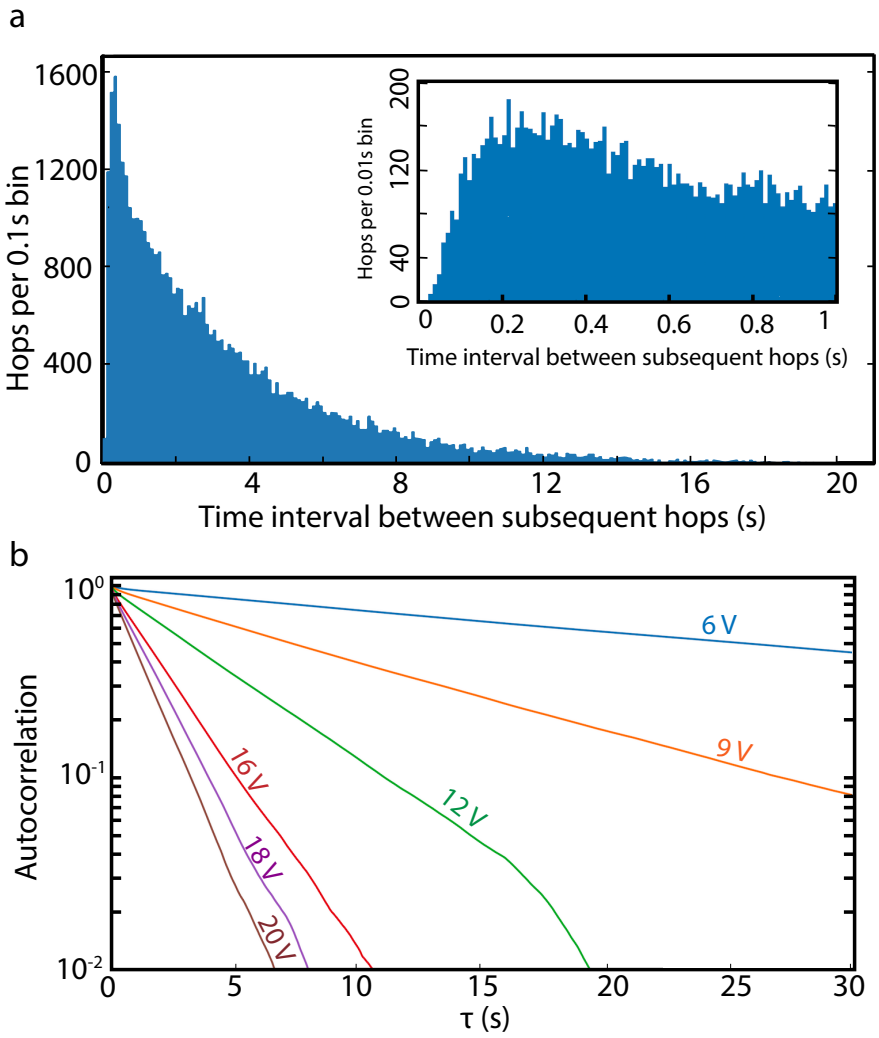

Figure 4.5: Statistics of simulated hopping trajectories. a) Distribution of time intervals between subsequent hops for a 100,000 s simulated trajectory with $\sigma_e = 20\,\mathrm{V}$. Inset: Short time detail of the same distribution. b) Autocorrelation of y position with τ for simulated trajectories with $\sigma_e = 6$, 9, 12, 16, 18, and 20 V.

Figure 4.5a shows the distribution of intervals between subsequent hops of a simulated molecule. The distribution shows an exponential decay on long time intervals (> 1 s), which is a hallmark of a noise-activated, barrier-crossing process. On short time intervals, there is a delay before the distribution exhibits a decaying character; the frequency of hopping intervals rises from zero to the peak value over the range 0 to 0.2 s. The finite time it takes a molecule to travel across the barrier explains that relative dearth of short hopping intervals.

Figure 4.5b plots the position autocorrelation, C_y, of a simulated particle as a function of the lag time, τ, for $\sigma_e = 6$, 9, 12, 16, 18, and 20 V. C_y decays exponentially with τ, and higher σ_e is associated with faster rate of decay. From the slopes of the curves in Fig. 4.5b, we find the characteristic decay times to be 35, 11, 4.6, 2.2, 1.7, and 1.4 s, ordered by increasing values of σ_e.

4.6 Concluding remarks

We have shown that it is possible to create a bi-stable fluidic device for a DNA molecule and controllably increase the DNA hopping rate between the two stable sites with artificial electrokinetic noise (Fig. 4.1). The resulting DNA hops correspond to thermally activated barrier crossing at an effective temperature that is adjustable well above temperatures that DNA can survive in (Fig. 4.4).

It is worth noticing that the actual thermal temperature was not changed; we confirmed using a thermocouple that the device temperature increased by only 0.1 C after an hour of applying the highest electrokinetic noise level, $\sigma_e = 22$ V. The curves in Fig.4.4 are experimental and simulation fits of the noise-induced hopping rate between the stable states using Arrhenius equation 4.6 with 2 fit parameters, attempt rate K_0 and barrier height $\Delta G^{\dagger}$.

The Arrhenius model explains the hopping rate of confined DNA polymers under electrokinetic noise reasonably well at low noise levels, but Fig. 4.6, 4.4, 4.5 are evidence that the Arrhenius model deviates significantly at higher noise levels. For example Fig. 4.6 highlights the significant amount of time that the DNA molecules spend between the stable sites at high noise level, which is not accounted for in the Arrhenius model. Fig. 4.4 shows that different sampling rates of the same simulated trajectories produce different parameters under the Arrhenius model. The inset of Fig. 4.5a shows the violation of the instantaneous transition assumption under Arrhenius model. The shortcomings of an Arrhenius model can be overcome with a numerical model that includes the extended energy landscape. Param-

eters of the free energy landscape used in the model can be obtained from Flory scaling theory; remarkably accurate predictions are obtained with a scaling pre-factor of 1. Additionally, the numerical simulations offered a way to study the DNA hopping dynamics on much shorter timescales (< 0.2 s) and longer timescales (> 60 s) than one can probe experimentally. We conclude that this numerical approach makes superior quantitative predictions of the dynamics and offers better theoretical insight into the noise-assisted hopping process for DNA.

This ability allows to study interesting noise driven phenomena. For example stochastic resonance (SR) is a general phenomenon that could be realized with a single DNA. As mentioned in chapter one, SR refers to the collaboration of white noise with a weak time varying signal in a bistable system where an optimum noise level enhances the effect of the weak signal. To experimentally study SR for a particle over an entropic barrier, one needs access to an extremely wide range of noise levels without varying the barriers height. The indicator of SR would be to see the synchronization between a weak periodic driving force and the hopping of the particle back and forth over an entropic barrier.

To explore SR for a DNA in a bistable potential, we simulated a Brownian particle in a similar bistable potential described earlier in the presence of a weak periodic pressure. Fig. 4.6 shows the simulated trajectories under different σs. First, we found a sub-threshold signal $p = 10$ mbars. At $\sigma = 0$ V, no jump was observed, confirming that $p = 10$ mbars is too weak to push the particle over the barrier. At a higher noise level, $\sigma = 5$ V, the particle hopped twice between the pits. We increased the noise level even higher to $\sigma = 10$ V, where the particle made several hops, around the peak amplitude of the applied pressure exhibiting stochastic resonance. At $\sigma = 15$ V, the particle appeared to hop back-and-forth frequently and randomly, displaying a stochastic motion. The hops at this noise level had no relation to the weak periodic force.

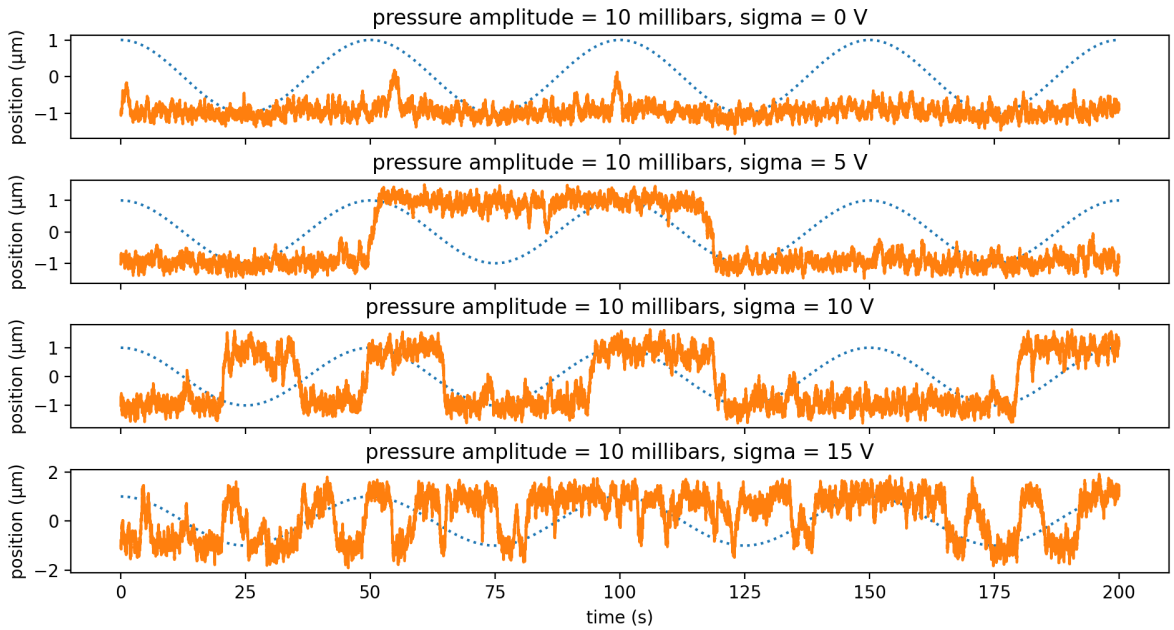

Figure 4.6: Stochastic Resonance: the addition of noise enhances the effect of a weak periodic driving force, and the DNA molecules hops back-and-forth at the same frequency as the force (collaboration with Tim Zhao).

There is also an opportunity to study how artificial noise influences the rates at which DNA molecules cross biologically relevant constrictions. In particular, passing DNA across barriers such as the blood-brain barrier [104–106] and endosomes [107–110] is a major obstacle in gene therapy. Electroporation is a technique of applying electric field pulses across a cell to increase the cell membrane permeability, which is a proven method of increasing the gene transfer efficiency in vivo and in vitro [111–113]. However, the strength of the electric field and the duration of exposure that cells can survive severely limits the technique; for example, tests on brain endothelial cells found the cell death grew increasingly likely as 50 ms electric field pulses increased beyond approximately 250 V/cm [105, 106]. We speculate that electrokinetic noise, whose strong electric fields have a mean of zero, may pose a relatively reduced risk to the cells, while the effect of increasing the barrier crossing rate might promote gene transfection. Fundamental research along these lines could lead to new biotechnologies and improved therapeutic methods.

Chapter 5

Viscosity Driven Drift of Nano-sized Particles in a Nanofluidic Environment

5.1 Theoretical foundation and previous work on transport in diffusivity gradients

So far the experiments in this dissertation took place in homogeneous solutions where diffusivity was a constant throughout the nanochannel. In this chapter we investigate the Brownian motion of suspended particles in nonhomgeneous media where the diffusivity is a linear function of the position. In this case, the dynamics of suspended particles are not easily predicted by the existing theories; depending on the integration convention the resulting dynamics are different. We refer to this ambiguity as the Itô-Stratonovich dilemma (explained in details in chapter 1.4).

Previous measurements of colloid dynamics in a diffusivity gradient in closed systems at equilibrium have confirmed the validity of the isothermal rule [28, 48, 114, 115]. In those studies, the hydrodynamic interactions between particles and a solid surface created a short-

ranged diffusivity gradient. Hydrodynamic interactions dampen the diffusivity as particles approach a surface causing an effective diffusivity gradient comparable to the particle size - and pointing away from the surface. The study by Lançon et al. [114] investigated the flux, confirming its absence in agreement with the isothermal rule. The colloidal particles drifted as predicted in the direction of increasing diffusivity, and the presence of a solid boundary ensured zero net particle flux Fig. 5.7.

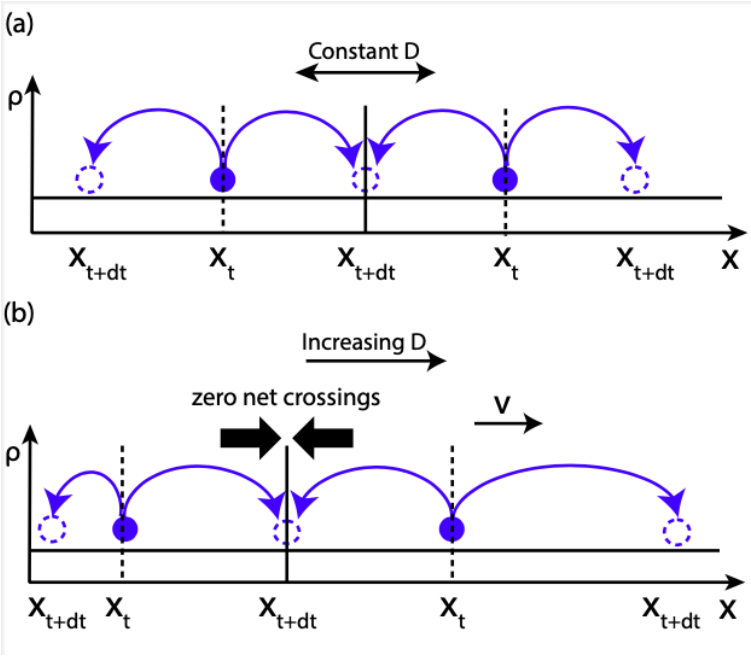

Figure 5.1: Stochastic displacement model corresponding to the isothermal rule a) illustrating the symmetric leftward and rightward steps of a random walker in the absence of a diffusivity gradient b) in a diffusivity gradient resulting in drift towards higher diffusivity and no net crossings (flux), corresponding to the isothermal rule.

In a recent series of experiments, Wiener et al. created a viscosity gradient by intermixing fluids of different viscosities within a nanofluidic channel and measured a steady current of ions in the channel. [116]. The viscosity gradient presumably created a diffusivity gradient for submerged particles according to Einstein's relation where D is related to the viscosity of the medium, η, by $D = \frac{k_B T}{6\pi\eta r}$, where $k_B T$ is the thermal energy and r is the hydrodynamic radius of the particle [33].

The steady measured current was evidently carried by counter ions drifting in the di-

rection of increasing diffusivity (decreasing viscosity). The measured current increased in proportion with the viscosity gradient along the nanochannel. The experiments by Wiener et al. differed from the previous experiments on Brownian motion in inhomogeneous media in at least three aspects. Firstly, constant mixing of fluids of different viscosities kept the system out of equilibrium and provided a source of free energy that could drive a non-zero flux of ions. Secondly, the length of the channel in which the viscosity gradient was established and the ionic current was measured significantly exceeded the submicrometer extent of the diffusivity gradient in the colloidal studies [28, 48, 114, 115].

Lastly, electrodes create unique boundary conditions, enabling ions to be absorbed at one end of the channel and new ions to be released from the other; the electrodes thus play a crucial role in supporting a steady current of ions, according to Wiener et al..

Wiener et al. used the Maxwell-Stefan model of diffusion to explain their results. The Maxwell-Stefan model is known to describe diffusion in multi-component systems that are out of equilibrium. However, the direct calculation of the drift velocity from the Maxwell-Stefan equation is difficult and it requires to solve nonlinear and coupled PDEs. As a result Maxwell-Stefan model is not as well understood compared to the Fick's model of diffusion that has been vastly studied [117–119].

In this chapter, we carry Wiener's work further by adding fluorescent particles inside a nanofluidic channel across which a controlled liquid viscosity gradient was imposed. We measure the diffusivity gradient throughout the channel by tracking the fluorescent particles, investigate the influence of the boundary conditions, and determine how well the nonintuitive isothermal model which predicts J=0 but v=dD/dx describes the Brownian motion of the suspended particles in our out of equilibrium system.

5.2 Experiment overview and methods

In our experiments the fluorescent particles experience reflective boundary conditions, and the ions experience electrode boundary conditions where electrodes at either end of the mixing nanochannel absorb and emit ions rather than reflecting them. An ion can get absorbed by an electrode on one side and released at the opposite electrode. This creates an effective circular loop for the channel which allows for flux of the ions.

We show that even in a system that is out of equilibrium and in the absence of electrode boundary condition for the fluorescent particles we observe net drift and no flux of the particles which agrees with the Isothermal model. While in Wiener's work, the diffusivity gradient was presumed as a result of the mixing fluids, recording the individual trajectories enabled us to independently measure and confirm the linearity of the diffusivity gradient across the channel.

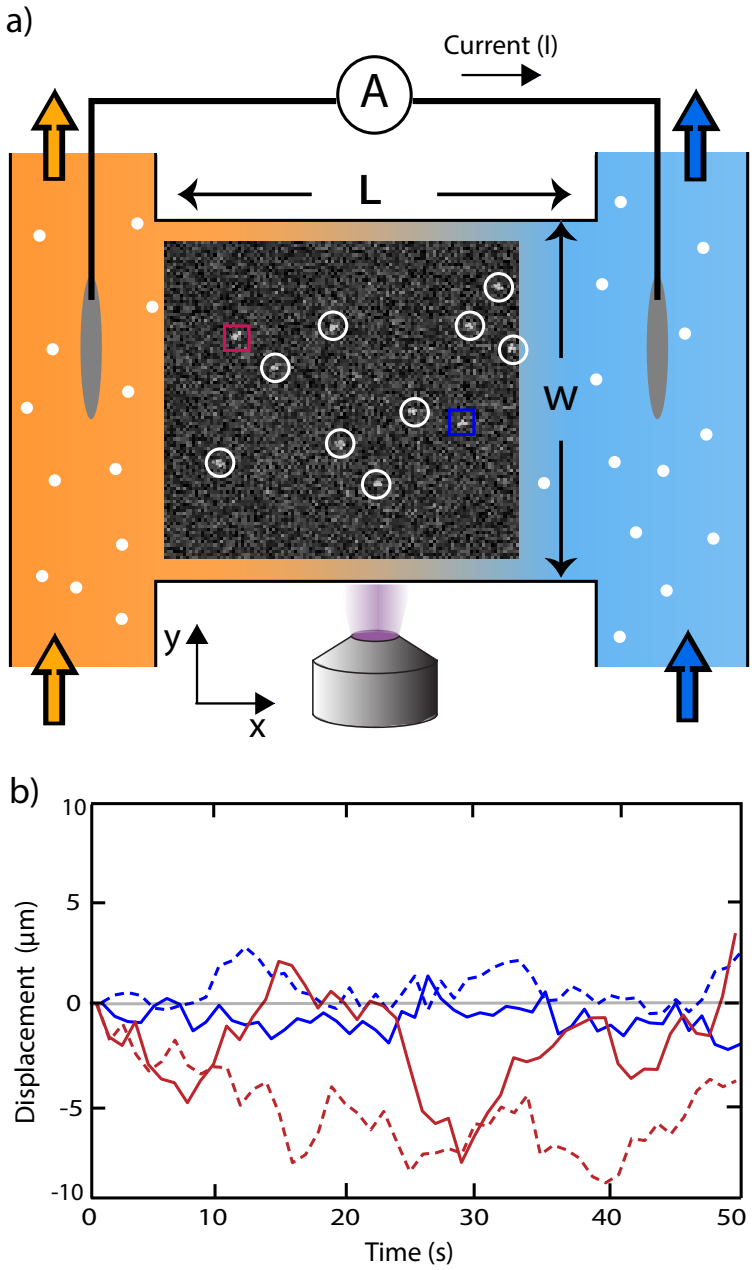

Figure 5.2: (a) Top view sketch of the mixing nanoslit between two microchannels. The flow of liquids of different viscosities at the ends of the mixing nanoslit creates a viscosity gradient along it. Objective lens captures the position of the fluospheres and the electrodes measure the current. (b) Sample trajectories of fluorescent particles in lower viscosity side (blue) and the higher viscosity side (orange) of the mixing channel. Solid lines show the x direction trajectory and dashed lines the y direction. The corresponding particles are marked in part (a)

“

Figure 5.2(a) illustrates the experimental setup. A glass nanofluidic chip with a 100 µm-long, 150 µm-wide, and 100 nm-deep mixing channel that bridged two 0.5 µm-deep U-shaped microchannels was fabricated using standard techniques described previously in chapter 2 and other publications [63, 64, 93]. At the start of each experiment, we introduced the same mixture into all four reservoirs and pumped the mixture through both microchannels. The microchannels were pumped by a constant 400 mbar pressure, to push each mixture from the reservoir through the channel. We measured the ionic current, I_v, flowing through the device. The homogeneous viscosity condition within the mixing channel resulted in a stable current close to zero. This was used as a sanity check. Next, a viscosity difference was imposed across the mixing channel by pumping liquids with different viscosities η_L and η_R through the left and right microchannels, respectively, as illustrated in Fig.5.2(a). The liquids were mixtures of glycerol, formamide, and aqueous solution containing 100 m KCl and 20 m borate buffer at pH 8.5. The buffer solution was held fixed at 50 % by volume in every mixture, while the relative amounts of formamide and glycerol were varied to adjust the viscosity ranging from 1.5 mPa s to 5.0 mPa s. We identify the mixtures by the glycerol content as a volume percentage for example 20%G contains 20% glycerol, 30% formamide and 50% of the buffer solution.

Glycerol is the most viscous component of all three, at 25 °C, the viscosity of glycerol (934 is), formamide's viscosity is (3.34 mPa s) and water (0.89 mPa s) [120]. We measured the mixture viscosities using a ball-drop technique described by Tang [121], the pH values using a Denver Instruments UB-10 pH meter, and the conductivities using a Hach EC-71 conductivity meter. We added approximately 2.2 μg/mL of fluorescent particles with a diameter of 0.04 μm (Invitrogen FluoSpheres carboxylate-modified microspheres, yellow-green fluorescent (505/515), 5 % solids, azide free) to each of the mixtures. The liquids are free to intermix within the nanochannel and establish a viscosity gradient. Every time a new liquid was substituted in one or both microchannels we waited for 30 minutes for the system to stabilize.

An ammeter (Axon Axopatch 200B) with Ag/AgCl electrodes immersed in the microchannels measured the ionic current, I_v, flowing through the fluidic chip. Next, to record videos of the fluorescent nanoparticles, the fluidic chip was placed on an optical microscope (Nikon TE2000-U). The microscope had a 100× oil immersion objective lens with a numerical aperture of 1.20, and an EMCCD camera (Andor iXon). A 120 W metal-halide lamp (EXFO X-Cite 120) supplied ultraviolet light for fluorescence imaging. A physical shutter (Uniblitz Model VCM-D1) was used to limit the exposure time and photo-bleaching of the fluorescent particles. Images were recorded with a 50 ms exposure time and intervals of $\Delta t = 250$ ms between the frames (4 frames per second). Figure 5.2(a) shows a sample image containing fluorescent particles.

A custom-written program identified the fluospheres and extracted the trajectories of their centers of mass (COM) from the sequence of images by computing the first moment of the particles' fluorescence intensity distributions. We enhanced the particle tracking method described previously [93] by distinguish momentarily overlapping particles based on their stable differences in their fluorescent intensity; the analysis code is publicly available [68]. Ensembles of trajectories enable measurements of particle drift, obtained by computing the mean inter-frame displacement per inter-frame time. As the amount of data (the number of steps) was increased, the effect of "noise" from the symmetric effect of diffusion gradually diminish, leaving the drift term. Ensembles of trajectories also enable measurements of flux, obtained by tallying the net crossings of a plane at fixed x as a function of time. The position dependent diffusivity of the particles was quantitatively determined by analyzing particle trajectories using a method developed by Frishman and Ronceray [122]. Frishman and Ronceray method applies to systems driven out of equilibrium by projecting the diffusivity profile on to an arbitrary polynomial basis; we used linear basis because we theoretically expect a linear diffusivity profile [116]. We estimated the local diffusion at a time t to be $\hat{d}(t) = \Delta x^2/2t$. We expanded $D(x)$ onto the normalized basis c_α, and approximate the coefficients as $\hat{D}_\alpha = \frac{1}{\tau}\sum_i \hat{d}(t_i)c_\alpha(x(t_i))\Delta t$ where τ is the total time. If we track 2 particles

each for 10 seconds, then τ would be 20 seconds.

We studied the flux of fluorescent particles in viscosity gradients by analyzing their trajectories. We tallied the net crossings of the planes $x = 10$, 40, and 70 μm as a function of time. The three planes provide independent measurements of the flux because a negligible number of particles crossed more than one plane (only 7 out of 2804 particles even in the most diffusive conditions with $\{0\,\%G, 0\,\%G\}$). Therefore, we assume the values of net crossings at different planes to be independent.

5.3 Results: fluorescent particles dynamics and ionic current.

Figure 5.2(b) shows two sample trajectories, one for a particle closer to the low-viscosity end and one closer to the high-viscosity end of the mixing channel. The particle closer to the low-viscosity end of the mixing channel fluctuates more extensively in both the x and y dimensions than the particle near the high-viscosity end.

Some of the particles get stuck on the surface of the fluidic chip. Figure 5.4 shows the histogram of the step size for the fluorescent particles. The stuck particles can be seen form the histogram. While the histogram has a Gaussian look the left side of the Gaussian exhibits an increase in the step sizes. We exclude the particles that have a smaller step size than 0.2 μ m. Figure 5.4 shows the remaining 6 histograms where they all exhibit the same general feature and a dip at 0.2 μ m.

Figure 5.5(a) shows the diffusivity profiles measured for different combinations of liquids in the microchannel. The diffusivity was relatively uniform in the nano channel when the microchannels on both sides contained the same liquid. We measured a diffusivity gradient when the microchannels contained different liquids. The diffusivity always increased in the direction of the decreasing glycerol content, and the magnitude of the diffusivity gradient increased in proportion to the viscosity difference imposed across the nanochannel. The

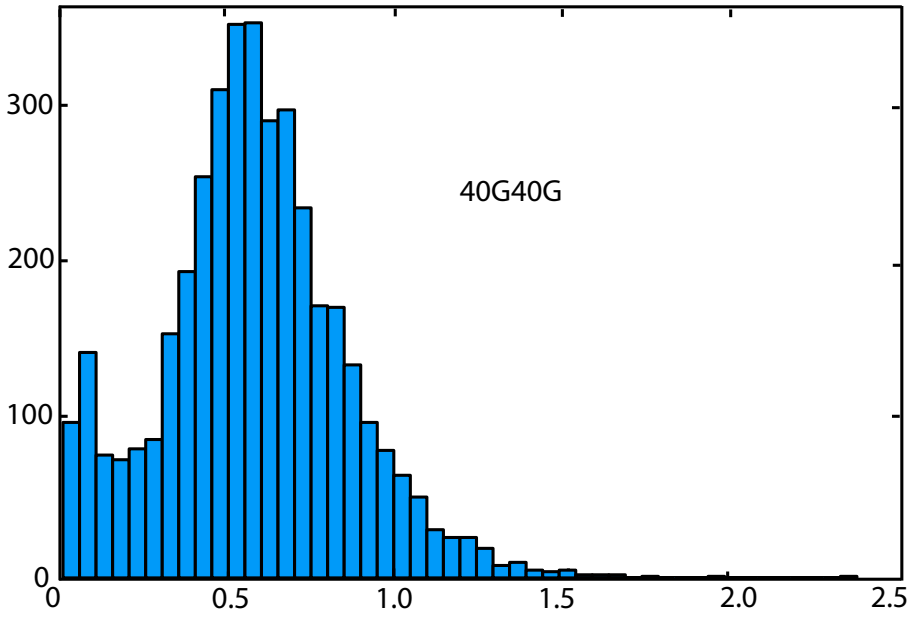

Figure 5.3: Histogram of step sizes for fluorescent particles for 40G40G mixture.

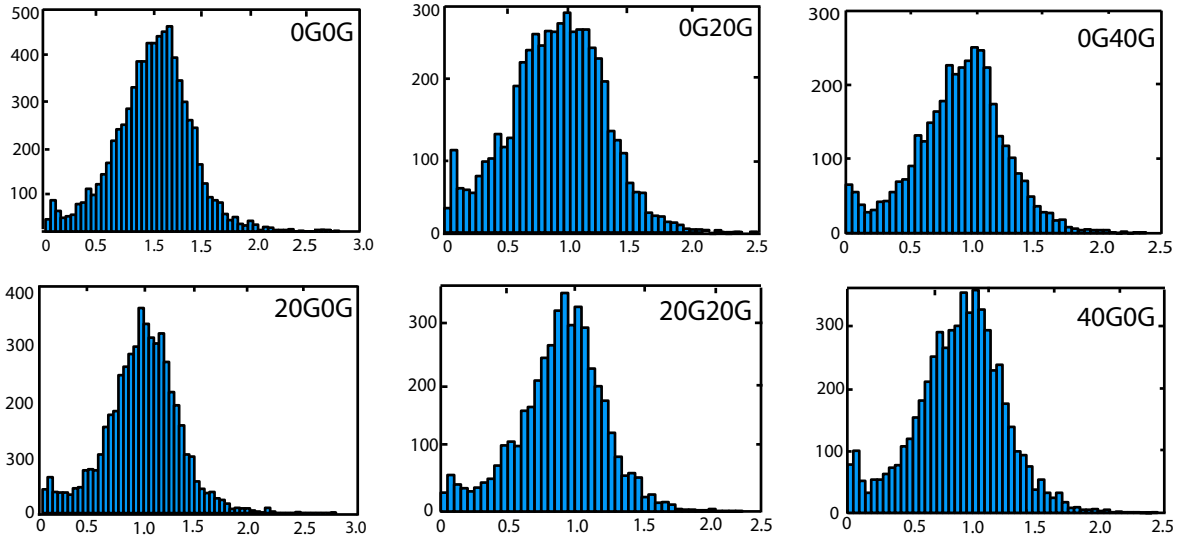

Figure 5.4: Histogram of step sizes for fluorescent particles for different mixture combinations.

average diffusivity for 0% glycerol was measured to be 7.2 $\mu m^2/s$, for 20% glycerol was 4.6 $\mu m^2/s$, and for 40% glycerol was 2.2 $\mu m^2/s$. The diffusivity gradient expected from the measured viscosities plot: The diffusivity line for $0\%G, 40\%G$ combination had a slope of -63, for $40\%, 0G\%$ combination had a slope of 73, for $20\%, 0G\%$ combination had a slope

of 49, and for $0\%, 20\%$ combination had a slope of -47. Remaking the mixtures resulted in slightly different viscosities since a small change in the amount of glycerol can cause a noticeable change in the viscosity of the mixture.

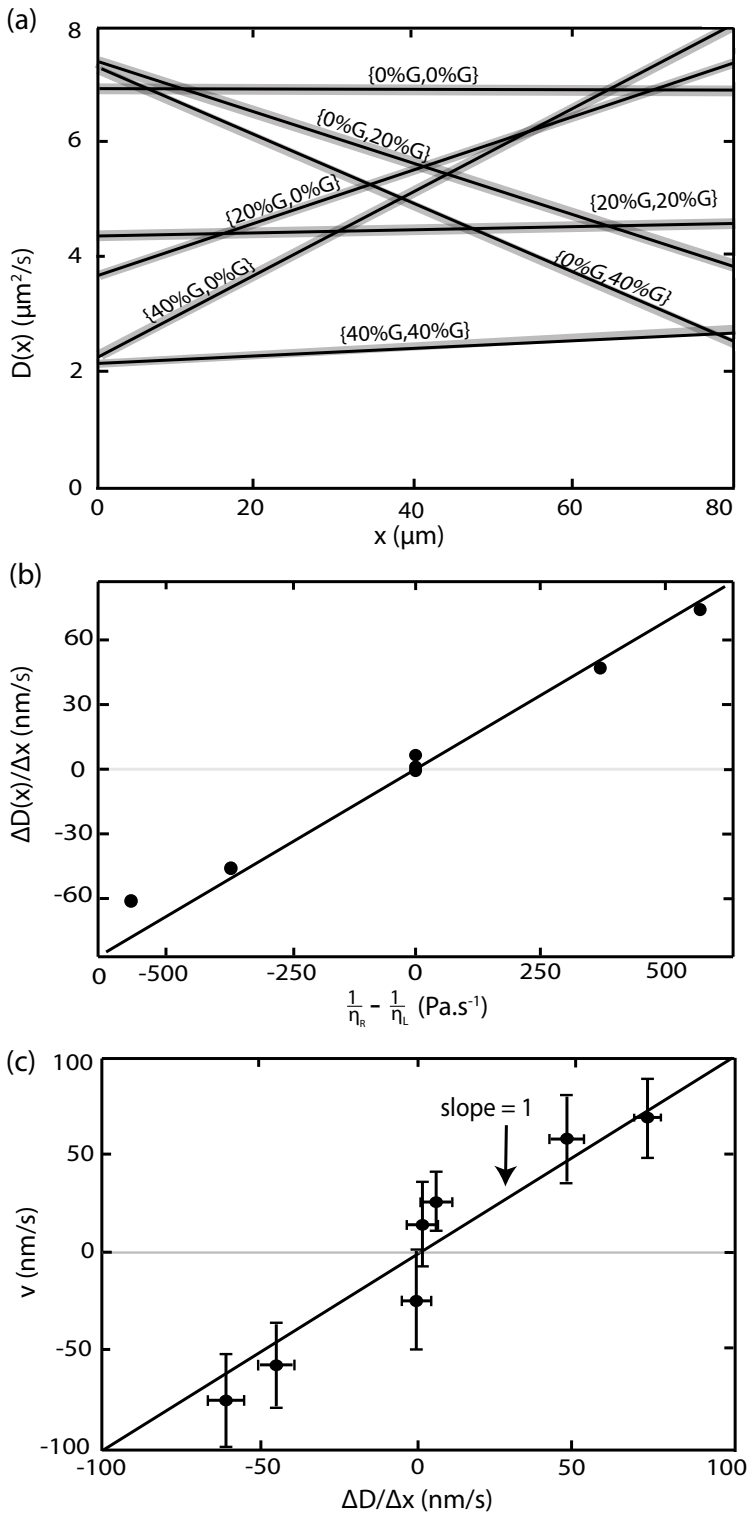

Figure 5.5: (a) Diffusivity profile within the mixing channel measured as the microchannels are flushed with liquids with viscosities η_L and η_R. We indicate the mixture combinations, $\{0\,\%G, 40\,\%G\}$, by the glycerol content in the {left, right} microchannels. $x = 0$ corresponds to the most left side of the channel Fig.5.2a). (b) Dependence of the diffusivity gradient on the difference in the inverse of imposed viscosities. The solid line is the prediction of the Stokes-Einstein relation, giving a slope of 1.36×10^{-16} J/nm. (c) Dependence of v on $\frac{\Delta D}{\Delta x}$. Error bars are the standard error of the mean.

Figure 5.5(b) shows the linear dependence of the diffusivity gradient measured inside the nanochannel on the difference of inverse viscosity imposed at either ends.

Figure 5.5(c) shows the relationship between v and the measured values of $\frac{\Delta D}{\Delta x}$. Each measurement of v synthesized between 5.5×10^4 and 8.0×10^4 inter-frame particle displacements. v increased from -74 ± 27 nm/s to $+71 \pm 23$ nm/s as $\frac{\Delta D}{\Delta x}$ increased over the similar range. v was close to zero when the viscosity in the channel was approximately uniform. Figure 5.5(c) compares the dependence of v on $\frac{\Delta D}{\Delta x}$ with the line predicted by the isothermal rule, $v = \frac{\Delta D}{\Delta x}$.

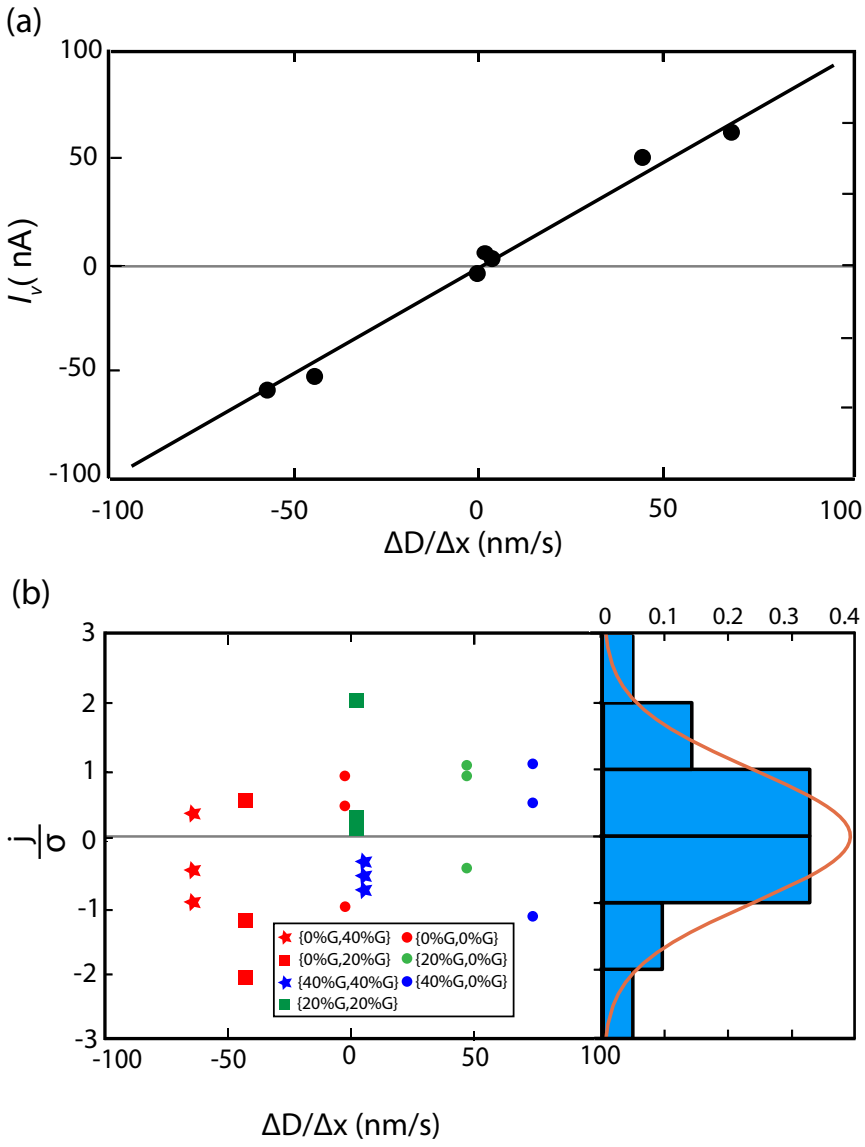

Figure 5.6: Current and flux measurements of viscophoresis (a) The dependence of $I_v\eta_L$ on $\Delta D/\Delta X$. solid line is the least square best fit. (b) Illustrates the number of standard deviations away the net crossings of the particles is from zero as a function of $\frac{\Delta D}{\Delta x}$. Each red dot represents j/σ through a plane for a specific mixture combination, averaged over all the videos. The histogram compares the normalized distribution of the j/σs to a normal Gaussian distribution.

Figure 5.6(a) shows the dependence of the ionic current on the diffusivity gradient; I_v is plotted against $\frac{\Delta D}{\Delta x}$. [116]. $I_v\eta_L$ is positive when $\frac{\Delta D}{\Delta x}. > 1$, it is negative when $\frac{\Delta D}{\Delta x}. < 1$, and its magnitude increased with the magnitude of $\frac{\Delta D}{\Delta x}$.

Figure 5.6(b) shows the mean flux of particles across the planes as a function of the dif-

fusivity gradient of the particles. The flux measurements were distributed around zero. The distribution is compared with a binomial distribution of mean zero and standard deviation σ given by $\sigma = \sqrt{npq}$, where $p = q = 1/2$ represent the equal probabilities of crossing a plane from the right or left, and n is the total number of crossings through that plane ($605 <$ n < 2436). All the flux values measured fell within 3σ of zero. n was smaller for the planes located at $x = 10$ and $x = 70$ since more particles escape the field of view (80 μm) during the course of a recording.

5.4 Discussion and interpretation

The diffusivity measurements in Fig. 5.5 confirm that imposing a viscosity difference across a nanochannel creates a linear diffusivity gradient within it. To a good approximation, the $D(x)$ profiles measured in Fig. 5.5(a) are simply lines connecting the diffusivity values for the liquids introduced in the left and right microchannels. Furthermore, Fig. 5.5(b) shows that the diffusivity gradient is in close agreement with the predictions of the Stokes-Einstein relation, $\frac{\Delta D}{L} = \frac{k_B T}{6\pi r L}(\frac{1}{\eta_R} - \frac{1}{\eta_L})$.

The measured drift of the fluorescent particles closely follows the spurious drift of a Brownian particle obeying the isothermal rule, as seen in the comparison of the measurements and the prediction $v = \frac{\Delta dD(x)}{\Delta x}$ in Figure 5.5(c). To establish the presence of a diffusivity gradient dependent drift, we constructed a hypothesis test based on $v =$ slope $\times(\Delta D/\Delta x)$. The null hypothesis we tested is that the true slope $= 0$. Our evidence against this null hypothesis is quantified in a p value that we computed from the slope of the least square fit to the measured data (1.11 ± 0.15) using a test statistic. The p value is then the probability of observing a slope of 1.11 or higher by random chance if the null hypothesis is true. With a p value $= 0.00001$ we reject the null hypothesis.

Remarkably, inside the same channel and under the same conditions, the flux of the fluorescent particles was consistent with zero while the ions experienced a net flux sourcing a

measurable current. The cause of the qualitative difference in the behavior of the two Brownian particles can be explained by the difference in the boundary conditions experienced. Only the ions can react chemically with the electrodes and get absorbed on one side and released on the other. The fluorescent particles experience a reflective boundary condition as illustrated in Fig. 5.7. We therefore deduce that the electrode boundary condition is essential for the flux of the ions.

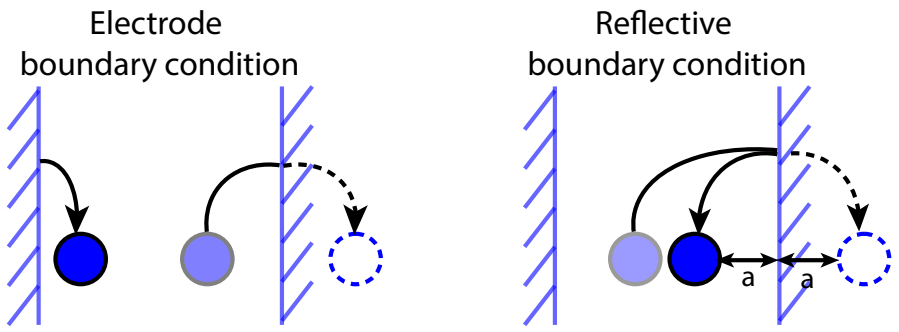

Figure 5.7: Illustrating the electrode boundary condition versus the reflective boundary condition.

Furthermore, the non-zero ionic flux shows that the ions are out of equilibrium. However, the dynamics of the fluorescent particles are still consistent with the isothermal description despite the system being held away from isothermal equilibrium by replenishing different, unmixed liquids on either side of the nanochannel. It is curious to know how far the system can be pushed out of equilibrium before the trajectories of the fluorescent particles also deviate from the isothermal equilibrium description. The accurate prediction of diffusion of mixtures is important to chemists, physicists, biologists, and engineers. However, it's not clear from the literature how far the Fick diffusion model (using the isothermal calculus) can be pushed away from equilibrium before it fails.

Chapter 6

Conclusions: Summary of what we learned, possible future work and open questions

This dissertation showed that nanofluidics provide an exceptional arena in which we can explore various noise driven dynamical phenomena in single molecular level. We showed that contrary to the traditional belief that noise is unwanted and an experimental nuisance, noise can play a beneficial role and under certain circumstances it is even useful to introduce noise to a system. Traditionally temperature has been used to control the noise in nanofluidic devices, but the range that temperature can be varied has practical limits. However, our technique to apply electrokinetic noise removes some of this limitation. The technique allowed us to increase the barrier crossing rate that is typically a fixed rate, for a DNA molecule without compromising the structural integrity of the DNA. According the Arrhenious' model, to increase the barrier crossing rate, one needs to decrease the ratio $\frac{\Delta G}{k_B T}$ While in enthalpic traps, increasing the temperature lowers the barrier height by increasing the activation energy, in entropic traps, the height of the barrier increases with the thermal noise and the entropic trapping becomes stronger. Our method to apply electrokinetic

noise allowed us to increase k_BT independently of ΔG. An ability to control the hopping rate of DNA across free energy barriers could open avenues for fundamental studies and biotechnological applications. For example, experimentally studying SR for DNA molecules over an entropic barrier. SR is an intriguing general phenomena in complex systems where under certain circumstances noise plays a constructive role. To do so, one needs access to an extremely wide range of noise levels for a trapped DNA molecule without varying the barrier height. Theory of SR was introduced about 40 years ago by Giorgio Parisi for understanding of the Earth's climate transitions from warm periods to ice ages [78]. Parisi was awarded a portion of 2021 Physics Nobel Prize "for the discovery of the interplay of disorder and fluctuations in physical systems from atomic to planetary scales".

Figure 6.1 illustrates SR where the addition of noise to a sub-threshold periodic signal can change the output. In part (A) when no noise is introduced, the signal remains below the recognition threshold and no output is registered. In part (B) in the presence of weak noise, small signal is registered. Part (C) shows the best signal representation when signal is combined with optimum level of noise. That is, each peak of the weak signal goes over the detection threshold, and an out put is registered. Part (D) shows that when high noise is introduced the output is random and indistinguishable from noise.

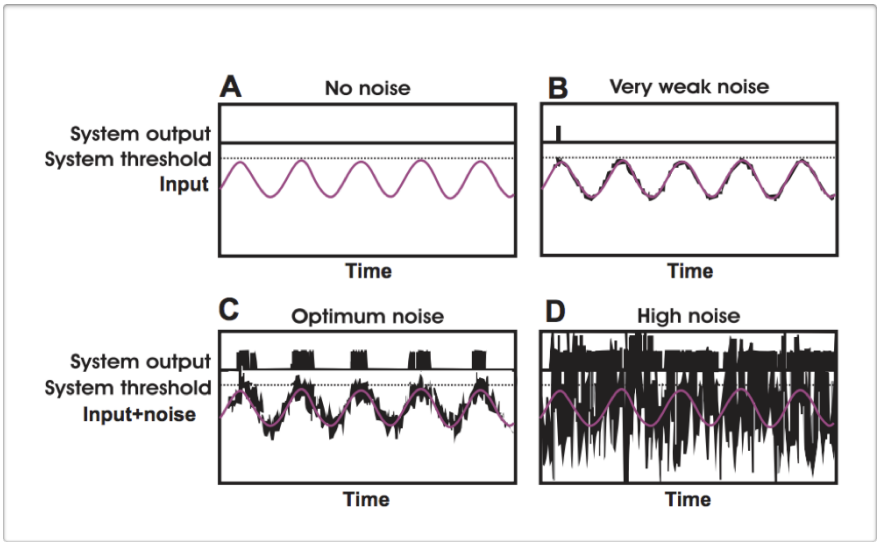

Figure 6.1: Weak signal in the presence of different noise intensities. A) no noise, B) very little noise, C) optimal noise (resonant), and D) high noise, Adopted from [123]

Chapter 3, and 4 controlled D by controlling the effective temperature but in chapter 5 D was manipulated through ζ. First, we illustrated that we can create a diffusivity gradient inside a nanochannel for submerged nano-particles by creating a gradient in ζ that depends on the imposed $\Delta\zeta$ across it.

The dynamics of the particles diffusing inside the viscosity gradient depended highly dependent on the boundary conditions. Particles experienced a drift or flux inside the viscosity gradient depending on the boundary conditions. Particles experiencing reflective boundary condition followed the isothermal equilibrium convention and experienced a drift equal to the diffusivity gradient along the nanochannel with no measurable flux. While the ions with electrode boundary condition experienced a net flux, exhibiting out of equilibrium dynamics. Viscosity gradients can be a used a a tool to drive transport for a variety of purposes in nanofluidics.

Across science and technology, many processes are based on diffusion and it is important to be able to predict the dynamics of diffusing particles in a given system. The Fick's model describes the dynamics of diffusing particles in the state of equilibrium and is well understood. However the Maxwell-Stefan model predicts the dynamics of systems that are

out of equilibrium but the mathematical properties of it are not fully understood.

Bibliography

[1] D. K. C. MacDonald, *Noise and fluctuations: an introduction*. Courier Corporation, 2006.

[2] T. Palmer, "Stochastic weather and climate models," *Nature Reviews Physics*, vol. 1, no. 7, pp. 463–471, 2019.

[3] M. GHIL, M. Kimoto, and J. Neelin, "Nonlinear dynamics and predictability in the atmospheric sciences," *Reviews of Geophysics*, vol. 29, no. S1, pp. 46–55, 1991.

[4] H. A. Dijkstra, "Nonlinear physical oceanography: a dynamical systems approach to the large scale ocean circulation and el nino," *Institute for Marine and Atmospheric Research Utrecht*, vol. 1, p. 2, 2005.

[5] A. BenSaïda, "A practical test for noisy chaotic dynamics," *SoftwareX*, vol. 3, pp. 1–5, 2015.

[6] F. Black, "Noise," *The journal of finance*, vol. 41, no. 3, pp. 528–543, 1986.

[7] G. E. Uhlenbeck and L. S. Ornstein, "On the theory of the brownian motion," *Physical review*, vol. 36, no. 5, p. 823, 1930.

[8] J. Christiansen and H. Kramers, "About the speed of chemical reactions," *Zeitschrift fur physical chemistry*, vol. 104, no. 1, pp. 451–471, 1923.

[9] H. A. Kramers, "Brownian motion in a field of force and the diffusion model of chemical reactions," *Physica*, vol. 7, no. 4, pp. 284–304, 1940.

[10] P. Hänggi, P. Talkner, and M. Borkovec, "Reaction-rate theory: fifty years after kramers," *Reviews of modern physics*, vol. 62, no. 2, p. 251, 1990.

[11] A. M. Selvam, "Noise or random fluctuations in physical systems: a review," *Self-organized Criticality and Predictability in Atmospheric Flows*, pp. 41–74, 2017.

[12] L. Gammaitoni, P. Hänggi, P. Jung, and F. Marchesoni, "Stochastic resonance," *Reviews of modern physics*, vol. 70, no. 1, p. 223, 1998.

[13] M. Asfaw and W. Sung, "Stochastic resonance of a flexible chain crossing over a barrier," *EPL (Europhysics Letters)*, vol. 90, no. 3, p. 30008, 2010.

[14] P. Hänggi, "Stochastic resonance in biology: How noise can enhance detection of weak signals and help improve biological information processing," *ChemPhysChem*, vol. 3, no. 3, pp. 285–290, 2002.

[15] Y. J. Kim, M. Grabowecky, and S. Suzuki, "Stochastic resonance in binocular rivalry," *Vision Research*, vol. 46, no. 3, pp. 392–406, 2006.

[16] Y. W. Kim and W. Sung, "Does stochastic resonance occur in periodic potentials?" *Physical Review E*, vol. 57, no. 6, p. R6237, 1998.

[17] J. Sharpe, N. Sungar, and N. Macaria, "Observation of stochastic resonance using an optically addressed amorphous silicon/ferroelectric liquid crystal spatial light modulator," *Optics communications*, vol. 114, no. 1-2, pp. 25–29, 1995.

[18] A. Grigorenko, P. Nikitin, and G. Roshchepkin, "Observation of stochastic resonance in a monostable magnetic system," *JETP Letters*, vol. 65, no. 10, pp. 828–832, 1997.

[19] A. Glukhov, A. Sivakov, and A. Ustinov, "Observation of stochastic resonance in percolative josephson media," *Low Temperature Physics*, vol. 28, no. 6, pp. 383–386, 2002.

[20] B. McNamara, K. Wiesenfeld, and R. Roy, "Observation of stochastic resonance in a ring laser," *Physical Review Letters*, vol. 60, no. 25, p. 2626, 1988.

[21] F. Moss, L. M. Ward, and W. G. Sannita, "Stochastic resonance and sensory information processing: a tutorial and review of application," *Clinical neurophysiology*, vol. 115, no. 2, pp. 267–281, 2004.

[22] B. McNamara and K. Wiesenfeld, "Theory of stochastic resonance," *Physical review A*, vol. 39, no. 9, p. 4854, 1989.

[23] A. Einstein, "On the motion of small particles suspended in liquids at rest required by the molecular-kinetic theory of heat," *Annalen der physik*, vol. 17, pp. 549–560, 1905.

[24] J. F. Brady, "Brownian motion, hydrodynamics, and the osmotic pressure," *The Journal of chemical physics*, vol. 98, no. 4, pp. 3335–3341, 1993.

[25] C. Bustamante, J. Marko, E. Siggia, and S. Smith, "Entropic elasticity of λ-phage DNA," *Proc. Nati. Acad. Sci USA*, vol. 88, p. 10009, 1991.

[26] S. Asakura and F. Oosawa, "On interaction between two bodies immersed in a solution of macromolecules," *The Journal of chemical physics*, vol. 22, no. 7, pp. 1255–1256, 1954.

[27] D. Rudhardt, C. Bechinger, and P. Leiderer, "Direct measurement of depletion potentials in mixtures of colloids and nonionic polymers," *Physical review letters*, vol. 81, no. 6, p. 1330, 1998.

[28] G. Volpe, L. Helden, T. Brettschneider, J. Wehr, and C. Bechinger, "Influence of noise on force measurements," *Physical review letters*, vol. 104, no. 17, p. 170602, 2010.

[29] F. Marchesoni, "Drift in diffusion gradients," *Materials*, vol. 6, no. 8, pp. 3598–3609, 2013.

[30] R. Brown, "On the particles contained in the pollen of plants; and on the general existence of active molecules in organic and inorganic bodies," *Edinburgh New Philosophical Journal*, vol. 5, pp. 358–371, 1828.

[31] R. P. Feynman, R. B. Leighton, and M. Sands, *The Feynman lectures on physics, Vol. I: The new millennium edition: mainly mechanics, radiation, and heat.* Basic books, 2011, vol. 1.

[32] P. Nelson, *Biological physics.* WH Freeman New York, 2004.

[33] A. Einstein, "äbout the motion of particles suspended in liquids at rest," *Annals of Physics*, vol. 4, 1905.

[34] M. Chaudesaigues, "Le mouvement brownien et la formule d'einstein," *Comptes rendus*, vol. 147, pp. 1044–1046, 1908.

[35] J. Perrin, "Mouvement brownien et réalité moléculaire," 1909.

[36] E. Frey and K. Kroy, "Brownian motion: a paradigm of soft matter and biological physics," *Annalen der Physik*, vol. 517, no. 1-3, pp. 20–50, 2005.

[37] P. Saffman and M. Delbrück, "Brownian motion in biological membranes." *Proceedings of the National Academy of Sciences*, vol. 72, no. 8, pp. 3111–3113, 1975.

[38] M. Kaszuba, D. McKnight, M. T. Connah, F. K. McNeil-Watson, and U. Nobbmann, "Measuring sub nanometre sizes using dynamic light scattering," *Journal of nanoparticle research*, vol. 10, no. 5, pp. 823–829, 2008.

[39] P. A. Hassan, S. Rana, and G. Verma, "Making sense of brownian motion: colloid characterization by dynamic light scattering," *Langmuir*, vol. 31, no. 1, pp. 3–12, 2015.

[40] R. N. Mantegna and H. E. Stanley, *Introduction to econophysics: correlations and complexity in finance.* Cambridge university press, 1999.

[41] J.-P. Bouchaud, M. Potters *et al.*, *Theory of financial risk and derivative pricing: from statistical physics to risk management*. Cambridge university press, 2003.

[42] L. Zhu and Y. Wang, "Rumor spreading model with noise interference in complex social networks," *Physica A: Statistical Mechanics and its Applications*, vol. 469, pp. 750–760, 2017.

[43] T. Chen, X. Yin, J. Yang, G. Cong, and G. Li, "Modeling multi-dimensional public opinion process based on complex network dynamics model in the context of derived topics," *Axioms*, vol. 10, no. 4, p. 270, 2021.

[44] N. G. Van Kampen and W. P. Reinhardt, "Stochastic processes in physics and chemistry," 1983.

[45] G. Volpe and J. Wehr, "Effective drifts in dynamical systems with multiplicative noise: a review of recent progress," *Reports on Progress in Physics*, vol. 79, no. 5, p. 053901, 2016.

[46] H. W. de Haan, M. V. Chubynsky, and G. W. Slater, "Monte carlo approaches for simulating a particle at a diffusivity interface and the" ito–stratonovich dilemma"," *arXiv preprint arXiv:1208.5081*, 2012.

[47] A. W. Lau and T. C. Lubensky, "State-dependent diffusion: Thermodynamic consistency and its path integral formulation," *Physical Review E*, vol. 76, no. 1, p. 011123, 2007.

[48] T. Brettschneider, G. Volpe, L. Helden, J. Wehr, and C. Bechinger, "Force measurement in the presence of brownian noise: Equilibrium-distribution method versus drift method," *Physical Review E*, vol. 83, no. 4, p. 041113, 2011.

[49] K. Itô, "109. stochastic integral," *Proceedings of the Imperial Academy*, vol. 20, no. 8, pp. 519–524, 1944.

[50] R. Stratonovich, "A new representation for stochastic integrals and equations," *Vestnik Mosk. Univ., Ser. I: Mat. Mekh.*, vol. 1, pp. 3–12, 1964.

[51] D. L. Fisk, "Quasi-martingales and stochastic integrals," Michigan State Univ East Lansing, Tech. Rep., 1963.

[52] P. Hanggi, "Nonlinear fluctuations: The problem of deterministic limit and reconstruction of stochastic dynamics," *Physical Review A*, vol. 25, no. 2, p. 1130, 1982.

[53] R. J. Meagher, A. V. Hatch, R. F. Renzi, and A. K. Singh, "An integrated microfluidic platform for sensitive and rapid detection of biological toxins," *Lab on a Chip*, vol. 8, no. 12, pp. 2046–2053, 2008.

[54] W. Volkmuth and R. Austin, "Dna electrophoresis in microlithographic arrays," *Nature*, vol. 358, no. 6387, pp. 600–602, 1992.

[55] S. Turner, A. Perez, A. Lopez, and H. Craighead, "Monolithic nanofluid sieving structures for dna manipulation," *Journal of Vacuum Science & Technology B: Microelectronics and Nanometer Structures Processing, Measurement, and Phenomena*, vol. 16, no. 6, pp. 3835–3840, 1998.

[56] J. Han and H. G. Craighead, "Separation of long DNA molecules in a microfabricated entropic trap array," *Science*, vol. 288, no. 5468, pp. 1026–1029, 2000.

[57] V. Müller and F. Westerlund, "Optical dna mapping in nanofluidic devices: principles and applications," *Lab on a Chip*, vol. 17, no. 4, pp. 579–590, 2017.

[58] S. Wang and L. J. Lee, "Micro-/nanofluidics based cell electroporation," *Biomicrofluidics*, vol. 7, no. 1, p. 011301, 2013.

[59] J. Hur and A. J. Chung, "Microfluidic and nanofluidic intracellular delivery," *Advanced Science*, vol. 8, no. 15, p. 2004595, 2021.

[60] N. Di Trani, A. Silvestri, A. Sizovs, Y. Wang, D. R. Erm, D. Demarchi, X. Liu, and A. Grattoni, "Electrostatically gated nanofluidic membrane for ultra-low power controlled drug delivery," *Lab on a Chip*, vol. 20, no. 9, pp. 1562–1576, 2020.

[61] J. Fu, J. Yoo, and J. Han, "Molecular sieving in periodic free-energy landscapes created by patterned nanofilter arrays," *Physical review letters*, vol. 97, no. 1, p. 018103, 2006.

[62] W. Reisner, N. B. Larsen, H. Flyvbjerg, J. O. Tegenfeldt, and A. Kristensen, "Directed self-organization of single DNA molecules in a nanoslit via embedded nanopit arrays," *Proceedings of the National Academy of Sciences*, vol. 106, no. 1, pp. 79–84, 2009.

[63] J. Del Bonis-O'Donnell, W. Reisner, and D. Stein, "Pressure-driven DNA transport across an artificial nanotopography," *New Journal of Physics*, vol. 11, no. 7, p. 075032, 2009.

[64] E. Shelton, Z. Jiang, S. Wang, and D. Stein, "Controlling the conformations and transport of dna by free energy landscaping," *Applied Physics Letters*, vol. 99, no. 26, p. 263112, 2011.

[65] D. Ross, E. A. Strychalski, C. Jarzynski, and S. M. Stavis, "Equilibrium free energies from non-equilibrium trajectories with relaxation fluctuation spectroscopy," *Nature Physics*, vol. 14, no. 8, pp. 842–847, 2018.

[66] A. Storm, J. Chen, X. Ling, H. Zandbergen, and C. Dekker, "Fabrication of solid-state nanopores with single-nanometre precision," *Nature materials*, vol. 2, no. 8, pp. 537–540, 2003.

[67] D. Kim, C. Bowman, J. T. Del Bonis-O'Donnell, A. Matzavinos, and D. Stein, "Giant acceleration of dna diffusion in an array of entropic barriers," *Physical Review Letters*, vol. 118, no. 4, p. 048002, 2017.

[68] "Amplification of dna brownian motion using electrokinetic noise data," https://doi.org/10.7910/DVN/OJHYZA.

[69] A. E. Cohen and W. Moerner, "Method for trapping and manipulating nanoscale objects in solution," *Applied physics letters*, vol. 86, no. 9, p. 093109, 2005.

[70] C. Miller, W. Daywitt, and M. Arthur, "Noise standards, measurements, and receiver noise definitions," *Proceedings of the IEEE*, vol. 55, no. 6, pp. 865–877, 1967.

[71] G. Szamel, "Self-propelled particle in an external potential: Existence of an effective temperature," *Physical Review E*, vol. 90, no. 1, p. 012111, 2014.

[72] M. Doi, *Soft matter physics*. Oxford University Press, 2013.

[73] S. Dattagupta, *Diffusion: Formalism and Applications*. CRC Press, 2013.

[74] T. M. Cover and J. A. Thomas, *Elements of information theory*. John Wiley & Sons, 2012.

[75] R. Pintelon, J. Schoukens, and P. Guillaume, "Continuous-time noise modeling from sampled data," *IEEE Transactions on Instrumentation and Measurement*, vol. 55, no. 6, pp. 2253–2258, 2006.

[76] K. D. Dorfman, D. Gupta, A. Jain, A. Muralidhar, and D. R. Tree, "Hydrodynamics of dna confined in nanoslits and nanochannels," *The European Physical Journal Special Topics*, vol. 223, no. 14, pp. 3179–3200, 2014.

[77] N. C. Stellwagen, C. Gelfi, and P. G. Righetti, "The free solution mobility of DNA," *Biopolymers: Original Research on Biomolecules*, vol. 42, no. 6, pp. 687–703, 1997.

[78] R. Benzi, G. Parisi, A. Sutera, and A. Vulpiani, "Stochastic resonance in climatic change," *Tellus*, vol. 34, no. 1, pp. 10–15, 1982.

[79] C. Battle, C. P. Broedersz, N. Fakhri, V. F. Geyer, J. Howard, C. F. Schmidt, and F. C. MacKintosh, "Broken detailed balance at mesoscopic scales in active biological systems," *Science*, vol. 352, no. 6285, pp. 604–607, 2016.

[80] D. Kim, C. Bowman, J. T. Del Bonis-O'Donnell, A. Matzavinos, and D. Stein, "Giant acceleration of DNA diffusion in an array of entropic barriers," *Phys. Rev. Lett.*, vol. 118, p. 048002, Jan 2017. [Online]. Available: https://link.aps.org/doi/10.1103/PhysRevLett.118.048002

[81] J. Spiechowicz, M. Kostur, and J. Łuczka, "Brownian ratchets: How stronger thermal noise can reduce diffusion," *Chaos: An Interdisciplinary Journal of Nonlinear Science*, vol. 27, no. 2, p. 023111, 2017.

[82] Y. Tan, J. Gladrow, U. F. Keyser, L. Dagdug, and S. Pagliara, "Particle transport across a channel via an oscillating potential," *Physical Review E*, vol. 96, no. 5, p. 052401, 2017.

[83] A. R. Klotz, B. W. Soh, and P. S. Doyle, "Motion of knots in dna stretched by elongational fields," *Physical review letters*, vol. 120, no. 18, p. 188003, 2018.

[84] A. McMullen, H. W. de Haan, J. X. Tang, and D. Stein, "Buckling causes nonlinear dynamics of filamentous viruses driven through nanopores," *Physical review letters*, vol. 120, no. 7, p. 078101, 2018.

[85] A. Ganopolski and S. Rahmstorf, "Abrupt glacial climate changes due to stochastic resonance," *Physical Review Letters*, vol. 88, no. 3, p. 038501, 2002.

[86] R. Benzi, "Stochastic resonance: from climate to biology," *Nonlinear Processes in Geophysics*, vol. 17, no. 5, pp. 431–441, 2010.

[87] J.-P. Bouchaud and R. Cont, "A langevin approach to stock market fluctuations and crashes," *The European Physical Journal B-Condensed Matter and Complex Systems*, vol. 6, no. 4, pp. 543–550, 1998.

[88] D. Valenti, B. Spagnolo, and G. Bonanno, "Hitting time distributions in financial markets," *Physica A: Statistical Mechanics and its Applications*, vol. 382, no. 1, pp. 311–320, 2007.

[89] P.-G. De Gennes, "Passive entry of a dna molecule into a small pore," *Proceedings of the National Academy of Sciences*, vol. 96, no. 13, pp. 7262–7264, 1999.

[90] M. Muthukumar, "Translocation of a confined polymer through a hole," *Physical Review Letters*, vol. 86, no. 14, p. 3188, 2001.

[91] G. Costantini and F. Marchesoni, "Threshold diffusion in a tilted washboard potential," *EPL (Europhysics Letters)*, vol. 48, no. 5, p. 491, 1999.

[92] P. Reimann, C. Van den Broeck, H. Linke, P. Hänggi, J. Rubi, and A. Pérez-Madrid, "Giant acceleration of free diffusion by use of tilted periodic potentials," *Physical review letters*, vol. 87, no. 1, p. 010602, 2001.

[93] D. Kim, C. Bowman, J. T. Del Bonis-O'Donnell, A. Matzavinos, and D. Stein, "Giant acceleration of DNA diffusion in an array of entropic barriers," *Phys. Rev. Lett.*, vol. 118, p. 048002, Jan 2017.

[94] A. Dinsmore, M. F. Hsu, M. Nikolaides, M. Marquez, A. Bausch, and D. Weitz, "Colloidosomes: selectively permeable capsules composed of colloidal particles," *Science*, vol. 298, no. 5595, pp. 1006–1009, 2002.

[95] X. Liu, M. M. Skanata, and D. Stein, "Entropic cages for trapping dna near a nanopore," *Nature communications*, vol. 6, no. 1, pp. 1–9, 2015.

[96] N. Laachi and K. D. Dorfman, "Dna electrophoresis in confined, periodic geometries: A new lakes-straits model," *The Journal of chemical physics*, vol. 133, no. 23, p. 12B605, 2010.

[97] S. Lameh, L. Ding, and D. Stein, "Controlled amplification of dna brownian motion using electrokinetic noise," *Phys. Rev. Applied*, vol. 14, p. 054042, Nov 2020.

[98] W. Reisner, N. Larsen, H. Flyvbjerg, J. O. Tegenfeldt, and A. Kristensen, "Directed self-organization of single dna molecules in a nanoslit via embedded nanopit arrays," *PNAS*, vol. 106, no. 1, pp. 79–84, 2009.

[99] A. Balducci, P. Mao, J. Han, and P. Doyle, "Double-stranded dna diffusion in slitlike nanochannels," *Macromolecules*, vol. 39, no. 18, pp. 6273–6281, 2006.

[100] D. Stein, F. van der Heyden, and C. Koopmans, Wiepke ad Dekker, "Pressure-driven transport of confined dna polymers in fluidic channels," *PNAS*, vol. 103, no. 43, pp. 15 853–15 858, 2006.

[101] J. Tang, S. L. Levy, D. W. Trahan, J. J. Jones, H. G. Craighead, and P. S. Doyle, "Revisiting the conformation and dynamics of dna in slitlike confinement," *Macromolecules*, vol. 43, no. 17, pp. 7368–7377, 2010.

[102] M. Doi and S. Edwards, *The Theory of Polymer Dynamics*. New York: Oxford University Press, 1986.

[103] P.-G. Gennes, *Scaling Concepts in Polymer Physics*. Ithaca, NY: Cornell University Press, 1979.

[104] W. M. Pardridge, "Blood–brain barrier delivery," *Drug discovery today*, vol. 12, no. 1-2, pp. 54–61, 2007.

[105] M. Hjouj, D. Last, D. Guez, D. Daniels, S. Sharabi, J. Lavee, B. Rubinsky, and Y. Mardor, "Mri study on reversible and irreversible electroporation induced blood brain barrier disruption," 2012.

[106] M. Bonakdar, E. M. Wasson, Y. W. Lee, and R. V. Davalos, "Electroporation of brain endothelial cells on chip toward permeabilizing the blood-brain barrier," *Biophysical journal*, vol. 110, no. 2, pp. 503–513, 2016.

[107] L. D. Cervia, C.-C. Chang, L. Wang, and F. Yuan, "Distinct effects of endosomal escape and inhibition of endosomal trafficking on gene delivery via electrotransfection," *PloS one*, vol. 12, no. 2, p. e0171699, 2017.

[108] S. A. Smith, L. I. Selby, A. P. Johnston, and G. K. Such, "The endosomal escape of nanoparticles: Toward more efficient cellular delivery," *Bioconjugate chemistry*, vol. 30, no. 2, pp. 263–272, 2018.

[109] I. M. Degors, C. Wang, Z. U. Rehman, and I. S. Zuhorn, "Carriers break barriers in drug delivery: endocytosis and endosomal escape of gene delivery vectors," *Accounts of chemical research*, vol. 52, no. 7, pp. 1750–1760, 2019.

[110] B. M. Bruininks, P. C. Souza, H. Ingolfsson, and S. J. Marrink, "A molecular view on the escape of lipoplexed dna from the endosome," *Elife*, vol. 9, p. e52012, 2020.

[111] T. Y. Tsong, "Electroporation of cell membranes," *Electroporation and electrofusion in cell biology*, pp. 149–163, 1989.

[112] J. C. Weaver, "Electroporation of cells and tissues," *IEEE transactions on plasma science*, vol. 28, no. 1, pp. 24–33, 2000.

[113] J. Gehl, "Electroporation: theory and methods, perspectives for drug delivery, gene therapy and research," *Acta Physiologica Scandinavica*, vol. 177, no. 4, pp. 437–447, 2003.

[114] P. Lançon, G. Batrouni, L. Lobry, and N. Ostrowsky, "Drift without flux: Brownian walker with a space-dependent diffusion coefficient," *EPL (Europhysics Letters)*, vol. 54, no. 1, p. 28, 2001.

[115] E. R. Dufresne, D. Altman, and D. G. Grier, "Brownian dynamics of a sphere between parallel walls," *EPL (Europhysics Letters)*, vol. 53, no. 2, p. 264, 2001.

[116] B. Wiener and D. Stein, "Electrokinetic current driven by a viscosity gradient," *arXiv preprint arXiv:1807.09106*, 2018.

[117] F. Salvarani, "From the boltzmann description for mixtures to the maxwell–stefan diffusion equations," *From Particle Systems to Partial Differential Equations*, pp. 355–379, 2019.

[118] F. Salvarani and A. J. Soares, "On the relaxation of the maxwell–stefan system to linear diffusion," *Applied Mathematics Letters*, vol. 85, pp. 15–21, 2018.

[119] X. Liu, S. K. Schnell, J.-M. Simon, P. Krüger, D. Bedeaux, S. Kjelstrup, A. Bardow, and T. J. Vlugt, "Diffusion coefficients from molecular dynamics simulations in binary and ternary mixtures," *International journal of thermophysics*, vol. 34, no. 7, pp. 1169–1196, 2013.

[120] W. M. Haynes, "Crc handbook of chemistry and physics," 2016.

[121] J. X. Tang, "Measurements of fluid viscosity using a miniature ball drop device," *Review of Scientific Instruments*, vol. 87, no. 5, p. 054301, 2016.

[122] A. Frishman and P. Ronceray, "Learning force fields from stochastic trajectories," *Physical Review X*, vol. 10, no. 2, p. 021009, 2020.

[123] L. M. Ward, S. M. Doesburg, K. Kitajo, S. E. MacLean, and A. B. Roggeveen, "Neural synchrony in stochastic resonance, attention, and consciousness." *Canadian Journal*

of Experimental Psychology/Revue canadienne de psychologie expérimentale, vol. 60, no. 4, p. 319, 2006.